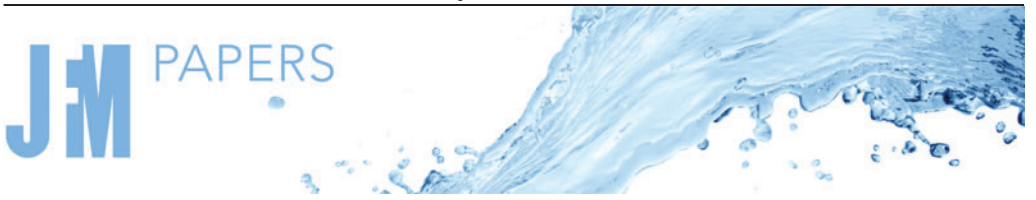
J. Fluid Mech. (2022), *vol*. 952, A25, doi:10.1017/jfm.2022.927



Improved modelling of interfacial terms in the second-moment closure for particle-laden flows based on interface-resolved simulation data

Yan Xia[1], **Zhaosheng Yu**[1],†, **Zhaowu Lin**[1] **and Yu Guo**[1]

[1]State Key Laboratory of Fluid Power and Mechatronic Systems, Department of Mechanics, Zhejiang University, Hangzhou 310027, PR China

(Received 12 July 2022; revised 30 October 2022; accepted 30 October 2022)

Correlations for the interfacial terms in the fluid dissipation rate equation and Reynolds stress equations are established for particle-laden flows, based on data from the interfaced-resolved direct numerical simulations of particle sedimentation in a periodic domain at a density ratio ranging from 0.01 to 1000, a particle concentration ranging from 2.3 % to 30.2 % and a particle Reynolds number below 250. The correlations for the mean drag and the pseudo-turbulent kinetic energy are also reported, which are used for the modelling of the interfacial term in the fluid dissipation rate equation. The interfacial term correlations obtained are then incorporated in the Reynolds stress model (RSM) (i.e. second-moment closure) for the simulation of vertical turbulent channel flows laden with the finite-size particles at relatively low particle volume fractions. The results show that the RSM with new interfacial term correlations can quantitatively predict particle-induced turbulence enhancement or suppression in vertical channel flows.

Key words: multiphase flow, particle/fluid flows, turbulence modelling

1. Introduction

Turbulent dispersed multiphase flows are encountered in many processes in nature and industry, such as fluidized beds, drug delivery, drilling process and sand storms. The two-fluid model (i.e. the Euler–Euler method) (Anderson & Jackson 1967; Ding & Gidaspow 1990; Ishii & Hibiki 2010) and the discrete particle (or element) model (i.e. the Euler–Lagrange method) (Tsuji, Kawaguchi & Tanaka 1993; Deen *et al.* 2007; Zhu *et al.* 2007) are two models widely used for particle-laden flows in engineering applications because of much lower computational resource requirements compared with direct numerical simulations (DNS). For the two-fluid model, modelling of the interphase

† Email address for correspondence: yuzhaosheng@zju.edu.cn

© The Author(s), 2022. Published by Cambridge University Press

https://doi.org/10.1017/jfm.2022.927 Published online by Cambridge University Press

	Politano *et al.* (2003)	Troshko & Hassan (2001)	Ma *et al.* (2017)	Yao & Morel (2004)	Rzehak & Krepper (2013)
Length scale	$k^{3/2}/\varepsilon$	d_p	d_p	$\lambda \sim d_p$	$k^{3/2}/\varepsilon$ or d_p
Velocity scale	$\sqrt{k}$	u_r	u_r	$(\varepsilon\lambda)^{1/3}$	u_r or $\sqrt{k}$
Time scale τ	k/ε	d_p/u_r	d_p/u_r	$d_p^{2/3}/\varepsilon^{1/3}$	$k^{3/2}/(\varepsilon u_r)$ or $d_p/\sqrt{k}$
$C_{\varepsilon 3}$	1.92	$1.35C_D$	$0.3C_D$	1.0	1.0

Table 1. Summary of characteristic scales for the modelling of the dissipation interfacial term based on dimensional analysis.

momentum and energy transfers is crucial for accurate simulations of industrial-scale multiphase flows (Crowe, Troutt & Chung 1996; Crowe *et al.* 2011; Joshi & Nandakumar 2015).

The turbulence models for particle-laden flows have been established based on the modification of single-phase turbulence models. In the past two decades numerous studies have been devoted to developing the two-equation multiphase turbulence models (including k–ε and k–ω) with transport equations for the turbulent kinetic energy (TKE) and dissipation rate (Sato & Hishida 1996; Troshko & Hassan 2001; Politano, Carrica & Converti 2003; Rzehak & Krepper 2013; Ma *et al.* 2017). Sato, Sadatomi & Sekoguchi (1981) proposed a particle-induced turbulence viscosity. The effects of particles on the turbulence can be captured through the inclusion of the interfacial (source) terms created by particles in the Reynolds stress and dissipation rate equations (Troshko & Hassan 2001; Politano *et al.* 2003; Rzehak & Krepper 2013; Fox 2014; Ma *et al.* 2017, 2020*b*). For the particle-induced turbulence, the interfacial term in the TKE equation, I_k, is generally modelled as the product of the interphase mean drag force per unit volume and the interphase mean slip velocity (Troshko & Hassan 2001; Colombo & Fairweather 2015; Mehrabadi *et al.* 2015; Ma *et al.* 2017).

The model of the interfacial term in the dissipation rate equation, I_ε, is much more complex. Based on dimensional analysis, a general expression of I_ε reads

$$I_\varepsilon = C_{\varepsilon 3}\frac{I_k}{\tau}, \tag{1.1}$$

where τ represents a characteristic time scale of the flow and $C_{\varepsilon 3}$ is an empirical coefficient. The determination of the characteristic scales for particle-laden flows is still a subject of debate in the literature because of the intrinsic multiscale property of particle-laden flows. Some typical choices of the characteristic scales and the coefficient $C_{\varepsilon 3}$ are summarized in table 1. For shear-dominated turbulence, the large-scale eddy time $\tau = k/\varepsilon$ is normally chosen as the characteristic time scale (Politano *et al.* 2003). For purely particle-induced pseudo-turbulence (i.e. the turbulence generated by the particles), the characteristic length scale is related to the wake length L_w or particle diameter d_p. Therefore, the time scale can be selected as $\tau = d_p/u_r$ (Troshko & Hassan 2001; Ma *et al.* 2017), where u_r is the particle slip velocity. Risso *et al.* (2008) suggested that $L_w \propto d_p/C_D$, while Du Cluzeau, Bois & Toutant (2019) argued that the wake length is in the range of $2d_p \sim 4d_p$. For the situation where both shear-induced turbulence and particle-induced turbulence are important, several hybrid scales have been proposed in the literature (Yao & Morel 2004; Rzehak & Krepper 2013).

The model of the dissipation rate interfacial term can also be derived from fundamentals. Schwarzkopf, Crowe & Dutta (2009) derived a dissipation rate transport

https://doi.org/10.1017/jfm.2022.927 Published online by Cambridge University Press

equation for particle-laden flows, and proposed a model of the dissipation rate interfacial term based on the point-particle approximation as

$$I_\varepsilon = C'_{\varepsilon 3}\frac{\nu^2}{V}\sum_k f_k \frac{|u_i - u_{pi}|_k^2}{d_p}, \tag{1.2}$$

where f_k is the drag factor, u_i and u_{pi} are the local fluid and particle velocities, respectively, and $C'_{\varepsilon 3}$ is an empirical coefficient. Experimental data on particle sedimentation in a quiescent fluid were used to obtain the coefficient $C'_{\varepsilon 3}$ for solid volume fractions between 10^{-6} and 10^{-2} and particle Reynolds numbers between 30 and 1000. The primary purpose of the present work is to provide an extending model for the solid volume fraction above 10^{-2}.

Although the two-equation models have been widely used to simulate multiphase flows, they fail to account for the strong anisotropy of particle-induced velocity fluctuations (Mehrabadi *et al.* 2015; Ma *et al.* 2020*b*). This limitation can be overcome by employing the Reynolds stress model (RSM) (Cokljat *et al.* 2006; Masood, Rauh & Delgado 2014; Capecelatro, Desjardins & Fox 2016*a*,*b*; Riella, Kahraman & Tabor 2019; Baker *et al.* 2020; Ma, Lucas & Bragg 2020*a*; Ma *et al.* 2020*b*; Shi & Rzehak 2020). For weakly inertial particle-laden flows, Capecelatro *et al.* (2016*b*) developed a multiphase RSM based on the data of point-particle DNS. The RSM framework has been used to simulate particle-laden vertical channel flows (Capecelatro *et al.* 2016*a*; Baker *et al.* 2020). Riella *et al.* (2019) proposed a pressure-velocity model for both particle and fluid phases that can account for the strong near-wall inhomogeneity of particle-laden channel flows. From experimental data on bubbly pipe flows, Colombo & Fairweather (2015) developed a RSM based on the Speziale–Sarkar–Gatski (SSG) model (Speziale, Sarkar & Gatski 1991) for bubble-induced turbulence.

In the past decades, interface-resolved (or particle-resolved) DNS (IR-DNS or PR-DNS) has been extensively employed to investigate the mechanisms in turbulence–particle interactions and the development of the multiphase turbulence model (Balachandar & Eaton 2010; Tenneti & Subramaniam 2014; Maxey 2017). Ma *et al.* (2017) for the first time used the IR-DNS data of bubble-induced turbulence in a vertical channel flow to develop the interfacial term models. In particular, a correlation of $C_{\varepsilon 3} = 0.3C_D$ is proposed, as shown in table 1, at the bubble volume fraction ranging from 1.07 % to 2.14 % and the bubble Reynolds number above 200. More recently, Ma *et al.* (2020*b*) extended this work in the framework of a second-moment closure for bubble-induced turbulence from DNS of dispersed bubbly flow in a vertical channel, and modelling of the pressure–strain term and the interfacial term in Reynolds stress equations was taken into consideration.

To our knowledge, the works on IR-DNS-based multiphase turbulence modelling are limited to bubble-induced turbulence at relatively low bubble volume fractions (Ma *et al.* 2017, 2020*b*). The IR-DNS data so far have not been used to develop a dissipation rate model for particle-laden flows. Thus, we aim to develop new models or correlations for the interfacial terms in the dissipation rate equation as well as in the Reynolds stress equations, based on interface-resolved simulations of particle sedimentation in a periodic domain at a density ratio ranging from 0.01 to 1000, a particle concentration ranging from 2.3 % to 30.2 % and a particle Reynolds number below 250. The correlations for the mean drag and the pseudo-TKE are also presented, which are required by the modelling of the interfacial term in the dissipation rate equation. In addition, the new models are employed in the RSM-based Reynolds-averaged Navier–Stokes (RANS) simulations of fully developed

https://doi.org/10.1017/jfm.2022.927 Published online by Cambridge University Press

vertical particle-laden channel flows. It is found that the model predictions are in good agreement with the DNS results for both turbulence enhancement and attenuation regimes.

The rest of the paper is organized as follows. In § 2 we address the basic equations of the RSM for the particle-laden flows. In § 3 we present the numerical method and the set-up for our interface-resolved simulations. Next, in § 4 the coefficients of the interfacial terms in the dissipation rate and Reynolds stress equations are determined on the basis of our DNS data. Then, in § 5 the proposed model is applied to RSM-based RANS simulations of vertical particle-laden channel flows, and the results are compared with the interface-resolved simulations. Concluding remarks are summarized in § 6.

2. Reynolds stress model

The averaged continuity and momentum equations of the Euler–Euler two-fluid approach for particle-laden flows (Anderson & Jackson 1967; Crowe *et al.* 2011) are

$$\frac{\partial(\phi_m\rho_m)}{\partial t}+\boldsymbol{\nabla}\cdot(\phi_m\rho_m\langle\boldsymbol{u}_m\rangle)=0, \tag{2.1}$$

$$\begin{aligned}\frac{\partial(\phi_f\rho_f\langle\boldsymbol{u}_f\rangle)}{\partial t}+\boldsymbol{\nabla}\cdot(\phi_f\rho_f\langle\boldsymbol{u}_f\rangle\langle\boldsymbol{u}_f\rangle)&=-\phi_f\boldsymbol{\nabla}\langle p_f\rangle+\boldsymbol{\nabla}\cdot(\phi_f\langle\boldsymbol{\tau}_f\rangle)\\&-\boldsymbol{\nabla}\cdot(\phi_f\rho_f\langle\boldsymbol{u}_f'\boldsymbol{u}_f'\rangle)+\phi_f\rho_f\boldsymbol{g}-\frac{1}{V}\int_{S_I}\boldsymbol{\sigma}_f\cdot\boldsymbol{n}\,\mathrm{d}s,\end{aligned} \tag{2.2}$$

$$\begin{aligned}\frac{\partial(\phi_s\rho_s\langle\boldsymbol{u}_s\rangle)}{\partial t}+\boldsymbol{\nabla}\cdot(\phi_s\rho_s\langle\boldsymbol{u}_s\rangle\langle\boldsymbol{u}_s\rangle)&=-\phi_s\boldsymbol{\nabla}\langle p_f\rangle+\boldsymbol{\nabla}\cdot(\phi_s\langle\boldsymbol{\sigma}_s\rangle)\\&-\boldsymbol{\nabla}\cdot(\phi_s\rho_s\langle\boldsymbol{u}_s'\boldsymbol{u}_s'\rangle)+\phi_s\rho_s\boldsymbol{g}+\frac{1}{V}\int_{S_I}\boldsymbol{\sigma}_f\cdot\boldsymbol{n}\,\mathrm{d}s.\end{aligned} \tag{2.3}$$

The subscript m in (2.1) denotes the phase (f denoting fluid phase and s solid phase). Here ρ, p, $\boldsymbol{u}$, $\boldsymbol{u}'$, $\boldsymbol{\tau}$ and $\boldsymbol{\sigma}$ represent the density, pressure, velocity, fluctuating velocity, viscous stress tensor and total stress tensor, respectively; $\langle\cdot\rangle$ represents phase averaging; ϕ_f and ϕ_s denote the mean volume fraction of fluid and solid phases, with $\phi_f+\phi_s=1.0$. The last term in (2.2) or (2.3) is the volume-averaged interphase hydrodynamic force, which may include the steady drag force, lift force and history force (Saffman 1956; Wen & Yu 1966; Antal, Lahey Jr & Flaherty 1991; Gidaspow 1994; Burns *et al.* 2004; Tenneti & Subramaniam 2014). Here we are only concerned with the steady mean drag force. In (2.2) the term $-\phi_f\rho_f\langle\boldsymbol{u}_f'\boldsymbol{u}_f'\rangle$ is the fluid Reynolds stress tensor. In (2.3), $\boldsymbol{\sigma}_s$ is the solid stress, including the solid pressure and shear stress, which are generally modelled by the kinetic theory of granular flows (Fox 2014).

The transport equations for the fluid-phase Reynolds stresses can be written as (Kataoka, Besnard & Serizawa 1992; Crowe *et al.* 2011; Peng, Ayala & Wang 2019)

$$\begin{aligned}\frac{\partial(\phi_f\rho_f\langle u_i'u_j'\rangle)}{\partial t}+\frac{\partial(\phi_f\rho_f\langle u_k\rangle\langle u_i'u_j'\rangle)}{\partial x_k}&=\underbrace{-\phi_f\rho_f(\langle u_i'u_k'\rangle\frac{\partial\langle u_j\rangle}{\partial x_k}+\langle u_j'u_k'\rangle\frac{\partial\langle u_i\rangle}{\partial x_k})}_{P_{ij}}\\&+D_{ij}+\Phi_{ij}-\varepsilon_{ij}+I_{ij}.\end{aligned} \tag{2.4}$$

Here and in the following, the subscript 'f' for the fluid velocity, pressure and stress is omitted for convenience, unless otherwise specified. The shear-induced production of Reynolds stresses, P_{ij}, can be determined without modelling. Here D_{ij}, ε_{ij}, Φ_{ij} and

https://doi.org/10.1017/jfm.2022.927 Published online by Cambridge University Press

I_{ij} represent the diffusion, pressure–strain term, dissipation term and interfacial term, respectively, and they need to be modelled for the second-moment closure. The diffusion term can be expressed as

$$D_{ij} = -\frac{\partial(\phi_f \rho_f \langle u_i' u_j' u_k' \rangle)}{\partial x_k} - \left[\frac{\partial(\phi_f \langle u_i' p' \rangle)}{z \partial x_j} + \frac{\partial(\phi_f \langle u_j' p' \rangle)}{\partial x_i} \right] + \left[\frac{\partial(\phi_f \langle u_i' \tau_{jk}' \rangle)}{\partial x_k} + \frac{\partial(\phi_f \langle u_j' \tau_{ik}' \rangle)}{\partial x_k} \right], \tag{2.5}$$

and can be modelled with the gradient diffusion hypothesis as (Shir 1973)

$$D_{ij} = \frac{\partial}{\partial x_k} \left[\phi_f \rho_f (\nu + c_s \nu_t) \frac{\partial \langle u_i' u_j' \rangle}{\partial x_k} \right], \tag{2.6}$$

where the eddy viscosity ν_t and an empirical coefficient c_s are introduced.

The dissipation term ε_{ij} can be expressed as

$$\varepsilon_{ij} = -\phi_f \left(\left\langle \tau_{ik}' \frac{\partial u_j'}{\partial x_k} \right\rangle + \left\langle \tau_{jk}' \frac{\partial u_i'}{\partial x_k} \right\rangle \right). \tag{2.7}$$

The isotropic model of $\varepsilon_{ij} = -\phi_f \rho_f \frac{2}{3} \delta_{ij} \varepsilon$ is widely used for high-Re turbulent flows, where ε is the average fluid-phase TKE dissipation rate. For low-Re wall-bounded flows, an anisotropic model proposed by Hanjalić & Launder (1976) is widely used, i.e.

$$\varepsilon_{ij} = \phi_f \rho_f \left(f_s \frac{\langle u_i' u_j' \rangle}{k} + \frac{2}{3}(1 - f_s) \delta_{ij} \right) \varepsilon, \tag{2.8}$$

where f_s is normally chosen as a constant or a function of the turbulent Reynolds number $Re_t = k^2/\varepsilon\nu$. For $f_s = 0$, ε_{ij} is isotropic, whereas for $f_s = 1$, ε_{ij} is fully anisotropic (Rotta 1951). For the particle-free channel flow, the DNS data of Kim, Moin & Moser (1987) and Mansour, Kim & Moin (1988) revealed that the dissipation tensor is strongly anisotropic with $f_s \approx 1$ close to the wall.

The pressure–strain term Φ_{ij} has the following form:

$$\Phi_{ij} = \phi_f \left\langle p' \frac{\partial u_i'}{\partial x_j} \right\rangle + \phi_f \left\langle p' \frac{\partial u_j'}{\partial x_i} \right\rangle. \tag{2.9}$$

The pressure–strain term plays a significant role in predicting the Reynolds stress anisotropy, and is most difficult for accurate modelling. It is generally modelled by the SSG model (Hanjalić & Launder 2011)

$$\Phi_{ij} = \Phi_{ij,1} + \Phi_{ij,2} + \Phi_{ij,3} + \Phi_{ij,w}, \tag{2.10}$$

where $\Phi_{ij,1}$, $\Phi_{ij,2}$, $\Phi_{ij,3}$ and $\Phi_{ij,w}$ represent the return to isotropy of turbulence (the slow term), isotropization of strain production (the rapid term), isotropization of force production and the wall blocking (Hanjalić & Launder 2011), respectively. The terms $\Phi_{ij,1}$

https://doi.org/10.1017/jfm.2022.927 Published online by Cambridge University Press

and $\Phi_{ij,2}$ are modelled as (Lumley 1979; Speziale *et al.* 1991)

$$\Phi_{ij,1} = -\phi_f \rho_f C_1 \varepsilon a_{ij} + \phi_f \rho_f C_1' \varepsilon (a_{ik}a_{kj} - \tfrac{1}{3}A_2\delta_{ij}), \tag{2.11}$$

$$\Phi_{ij,2} = -\phi_f \rho_f C_2 (P_{ij} - \tfrac{2}{3}P_k\delta_{ij}) - \phi_f \rho_f C_4 (E_{ij} - \tfrac{2}{3}P_k\delta_{ij}) - \phi_f \rho_f (0.033 + 0.65A_2^{1/2}) k S_{ij} - \phi_f \rho_f C_1^* a_{ij} P_k. \tag{2.12}$$

The isotropization of force production $\Phi_{ij,3}$ can be modelled as (Naot 1970)

$$\Phi_{ij,3} = -C_3 (I_{ij} - \tfrac{2}{3}I_k\delta_{ij}). \tag{2.13}$$

In the above equations, a_{ij} is the fluid Reynolds stress anisotropy tensor

$$a_{ij} = \frac{1}{k}\left(\langle u_i' u_j' \rangle - \frac{2}{3}k\delta_{ij}\right), \tag{2.14}$$

and $A_2 = a_{ji}a_{ij}$ is the second invariant of a_{ij}. The coefficients C_1, C_1', C_2, C_3, C_4 and C_1^* are model coefficients; P_k represents the TKE production rate; E_{ij} and S_{ij} are given as

$$E_{ij} = -\left[\langle u_i' u_k' \rangle \frac{\partial \langle u_k \rangle}{\partial x_j} + \langle u_j' u_k' \rangle \frac{\partial \langle u_k \rangle}{\partial x_i}\right], \tag{2.15}$$

$$S_{ij} = \frac{1}{2}\left(\frac{\partial \langle u_i \rangle}{\partial x_j} + \frac{\partial \langle u_j \rangle}{\partial x_i}\right). \tag{2.16}$$

The Reynolds stress interfacial term I_{ij} can be expressed as

$$I_{ij} = -\frac{1}{V}\left[\int_{S_I} n_k u_i' (-p'\delta_{jk} + \tau_{jk}')\,\mathrm{d}s + \int_{S_I} n_k u_j' (-p'\delta_{ik} + \tau_{ik}')\,\mathrm{d}s\right], \tag{2.17}$$

where S_I is the interphase surface inside the averaging volume. Neglecting the effect of the particle rotation, Crowe *et al.* (2011) derived the following form for the interfacial term:

$$I_{ij} = \frac{1}{V}\sum_k^{N_p} (\langle u_i \rangle - u_{pk,i}) F_{k,j} + \frac{1}{V}\sum_k^{N_p} (\langle u_j \rangle - u_{pk,j}) F_{k,i}. \tag{2.18}$$

Here $u_{pk,i}$ denotes the ith velocity component of the kth particle, N_p denotes the number of particles in the volume V and $F_{k,i}$ represents the drag force on the kth particle. Xia *et al.* (2022*a*) showed that, for the TKE interfacial term at the steady state, the term related to the particle rotation and the correlation between the particle fluctuating velocity and the drag force are negligibly small. Thus, the interfacial term (2.18) can reduce to

$$I_{ij} = F_{Di} u_{rj} + F_{Dj} u_{ri}, \tag{2.19}$$

where F_D is the volume-averaged drag and u_r represents the mean interphase slip velocity. On the other hand, it is conventional to establish the model of the Reynolds stress interfacial term with the TKE interfacial term I_k (Ma *et al.* 2020*b*)

$$I_{ij} = b_{ij} I_k, \tag{2.20}$$

where b_{ij} is a coefficient matrix. The Troshko–Hassan model (Troshko & Hassan 2001) is one of widely used models for the TKE interfacial term,

$$I_k = \boldsymbol{F}_D \cdot \boldsymbol{u}_r. \tag{2.21}$$

It was suggested to multiply (2.21) by a correction coefficient C_n, i.e. $I_k = C_n \boldsymbol{F}_D \cdot \boldsymbol{u}_r$. In the ANSYS FLUENT software, a value of 0.75 is recommended for C_n (Ansys, Inc

https://doi.org/10.1017/jfm.2022.927 Published online by Cambridge University Press

2013). Here C_n was determined as a function of TKE or particle Reynolds number from DNS of bubbly flows (Santarelli, Roussel & Fröhlich 2016; Ma *et al.* 2017) and as a function of the particle Reynolds number, the particle size, the density ratio and the particle volume fraction, based on the DNS data on the upward turbulent channel flow (Yu *et al.* 2021). However, we have recently demonstrated that C_n=1 is a better choice for the particle-laden flows at a statistically steady state (Xia *et al.* 2022*a*), being consistent with the observation of Mehrabadi *et al.* (2015). For the particle sedimentation in a periodic domain or in a vertical channel flow considered in the present study, the mean drag and the mean slip velocity are only non-zero in the vertical direction, thus, $I_{11} = 2I_k$ and the other components are zero. Accordingly, the only non-zero component of b_{ij} is $b_{11} = 2.0$.

The transport equation of the fluid-phase TKE reads

$$\frac{\partial(\phi_f\rho_f k)}{\partial t} + \frac{\partial(\phi_f\rho_f\langle u_j\rangle k)}{\partial x_j} = \underbrace{-\phi_f\rho_f\langle u_i'u_j'\rangle\frac{\partial\langle u_i\rangle}{\partial x_j}}_{P_k}$$
$$+ \underbrace{\frac{\partial}{\partial x_k}\left[\phi_f\rho_f(\nu + c_s\nu_t)\frac{\partial k}{\partial x_k}\right]}_{D_k} - \underbrace{\phi_f\rho_f\varepsilon}_{\varepsilon_k} + I_k, \tag{2.22}$$

where P_k and D_k represent the production and the diffusion of TKE, and ε_k is the dissipation term of TKE.

The transport equation for the dissipation rate ε is given as

$$\frac{\partial(\phi_f\rho_f\varepsilon)}{\partial t} + \frac{\partial(\phi_f\rho_f\langle u_j\rangle\varepsilon)}{\partial x_j} = \underbrace{-\phi_f\rho_f C_{\varepsilon1}\frac{\varepsilon}{k}\langle u_i'u_j'\rangle\frac{\partial\langle u_i\rangle}{\partial x_j}}_{P_\varepsilon}$$
$$+ \underbrace{\frac{\partial}{\partial x_j}\left(\phi_f\rho_f\left(\nu + \frac{\nu_T}{\sigma_\varepsilon}\right)\frac{\partial\varepsilon}{\partial x_j}\right)}_{D_\varepsilon} - \underbrace{C_{\varepsilon2}\phi_f\rho_f\frac{\varepsilon^2}{k}}_{\varepsilon_\varepsilon} + I_\varepsilon. \tag{2.23}$$

Here P_ε, D_ε and ε_ε represent the production, diffusion and dissipation of TKE dissipation rate, respectively; I_ε is the interfacial term in the ε equation; $C_{\varepsilon1}$, $C_{\varepsilon2}$ and σ_ε are model constants.

3. Numerical method and DNS setup

3.1. *Direct forcing/fictitious domain method*

The IR-DNS approach used in this work is the direct forcing/fictitious domain (DF/FD) method (Yu & Shao 2007; Yu *et al.* 2016). The key idea of this method is to fill the interior domain of solid particles with fictitious fluids, and introduce a pseudo-body force (i.e. distributed Lagrange multiplier Glowinski *et al.* 1999) over the solid region to enforce the rigid-body constraints. For simplicity of description, we consider only one particle in the following formulae. Let $P(t)$ represent the solid domain and Ω represents the entire domain including both the interior and exterior of the solid body. The particle density, volume and moment of inertia tensor, translational velocity and angular velocity are denoted by ρ_s, V_p, $\boldsymbol{J}$, $\boldsymbol{U}$ and $\boldsymbol{\omega}_p$, respectively. The viscosity and density of the fluid are μ and ρ_f.

https://doi.org/10.1017/jfm.2022.927 Published online by Cambridge University Press

We introduce the following characteristic scales for the non-dimensionalization: L_c for length, U_c for velocity, L_c/U_c for time, $\rho_f U_c^2/L_c$ for the body force. Then the dimensionless FD formulation for incompressible fluid can be written as

$$\frac{\partial \boldsymbol{u}}{\partial t} + \boldsymbol{u}\cdot\nabla\boldsymbol{u} = \frac{\nabla^2\boldsymbol{u}}{Re} - \nabla p + \boldsymbol{\lambda} \text{ in } \Omega, \tag{3.1}$$

$$\boldsymbol{u} = \boldsymbol{U} + \boldsymbol{\omega}_p \times \boldsymbol{r} \text{ in } P(t), \tag{3.2}$$

$$\nabla\cdot\boldsymbol{u} = 0 \text{ in } \Omega, \tag{3.3}$$

$$(\rho_r - 1)V_p^*\left(\frac{\mathrm{d}\boldsymbol{U}}{\mathrm{d}t} - Fr\frac{\boldsymbol{g}}{g}\right) = -\int_P \boldsymbol{\lambda}\,\mathrm{d}\boldsymbol{x}, \tag{3.4}$$

$$(\rho_r - 1)\frac{\mathrm{d}(\boldsymbol{J}^*\cdot\boldsymbol{\omega}_p)}{\mathrm{d}t} = -\int_P \boldsymbol{r}\times\boldsymbol{\lambda}\,\mathrm{d}\boldsymbol{x}, \tag{3.5}$$

where $\boldsymbol{u}$, p and $\boldsymbol{\lambda}$, $\boldsymbol{r}$ represent the fluid velocity, pressure, pseudo-body force and position vector with respect to the mass centre of the particle, respectively. Here ρ_r is the particle–fluid density ratio defined by $\rho_r = \rho_s/\rho_f$, Re the Reynolds number defined by $Re = \rho_f U_c L_c/\mu$ and Fr is the Froude number defined by $Fr = gL_c/U_c^2$, with g being the gravitational acceleration; V_p^* and $\boldsymbol{J}^*$ are the dimensionless particle volume and moment of inertia tensor, defined by $V_p^* = V_p/L_c^3$ and $\boldsymbol{J}^* = \boldsymbol{J}/\rho_s L_c^5$.

A fractional-step temporal scheme is used to decouple the system (3.1)–(3.5) into two subproblems.

(1) The fluid subproblem for $\boldsymbol{u}^*$ and p is given by

$$\frac{\boldsymbol{u}^* - \boldsymbol{u}^n}{\Delta t} - \frac{1}{2}\frac{\nabla^2\boldsymbol{u}^*}{Re} = -\nabla p - \frac{1}{2}[3(\boldsymbol{u}\cdot\nabla\boldsymbol{u})^n - (\boldsymbol{u}\cdot\nabla\boldsymbol{u})^{n+1}] + \frac{1}{2}\frac{\nabla^2\boldsymbol{u}^n}{Re} + \boldsymbol{\lambda}^n, \tag{3.6}$$

$$\nabla\cdot\boldsymbol{u}^* = 0. \tag{3.7}$$

A finite-difference-based projection method on a homogeneous half-staggered grid is used. All spatial derivatives are discretized with a second-order central difference scheme.

(2) The particle subproblem for $\boldsymbol{U}^{n+1}$, $\boldsymbol{\omega}_p^{n+1}$, $\boldsymbol{\lambda}^{n+1}$ and $\boldsymbol{u}^{n+1}$ is given by

$$\rho_r V_p^*\frac{\boldsymbol{U}^{n+1}}{\Delta t} = (\rho_r - 1)V_p^*\left(\frac{\boldsymbol{U}^n}{\Delta t} - Fr\frac{\boldsymbol{g}}{g}\right) + \int_P\left(\frac{\boldsymbol{u}^*}{\Delta t} - \boldsymbol{\lambda}^n\right)\mathrm{d}\boldsymbol{x}, \tag{3.8}$$

$$\rho_r\frac{\boldsymbol{J}^*\cdot\boldsymbol{\omega}_p^{n+1}}{\Delta t} = (\rho_r - 1)\left[\frac{\boldsymbol{J}^*\cdot\boldsymbol{\omega}_p^n}{\Delta t} - \boldsymbol{\omega}_p^n\times(\boldsymbol{J}^*\cdot\boldsymbol{\omega}_p^n)\right] + \int_P \boldsymbol{r}\times\left(\frac{\boldsymbol{u}^*}{\Delta t} - \boldsymbol{\lambda}^n\right)\mathrm{d}\boldsymbol{x}. \tag{3.9}$$

The pseudo-body forces $\boldsymbol{\lambda}$ are then updated from

$$\boldsymbol{\lambda}^{n+1} = \frac{\boldsymbol{U}^{n+1} + \boldsymbol{\omega}_p^{n+1}\times\boldsymbol{r} - \boldsymbol{u}^*}{\Delta t} + \boldsymbol{\lambda}^n. \tag{3.10}$$

Finally, the fluid velocities $\boldsymbol{u}^{n+1}$ at the Eulerian nodes are corrected as

$$\boldsymbol{u}^{n+1} = \boldsymbol{u}^* + \Delta t(\boldsymbol{\lambda}^{n+1} - \boldsymbol{\lambda}^n). \tag{3.11}$$

In the above manipulations, a discrete δ function in the form of a trilinear function is employed to transfer quantities between the Eulerian and Lagrangian nodes.

https://doi.org/10.1017/jfm.2022.927 Published online by Cambridge University Press

3.2. Collision model

We implement a soft-sphere collision model with lubrication correction to solve the short-ranged inter-particle interaction. A discrete element model based on a nonlinear soft-sphere approach is coupled to our DF/FD solver. The total contact force acting on particle i by another particle j is described by

$$\boldsymbol{F}_{ij,n} = (-k_n\delta_n^{3/2} - \eta_n\boldsymbol{u}_{ij}\cdot\boldsymbol{n})\boldsymbol{n}, \tag{3.12}$$

$$\boldsymbol{F}_{ij,t} = (-k_t\delta_t - \eta_t\boldsymbol{u}_{ij,t}\cdot\boldsymbol{t})\boldsymbol{t}, \tag{3.13}$$

where $\boldsymbol{F}_{ij,n}$, δ_n, k_n and η_n are the normal contact force, overlapping distance, stiffness coefficient and damping coefficient, respectively, and $\boldsymbol{F}_{ij,t}$, δ_t, k_t, η_t are the corresponding parameters in the tangential direction. Also, $\boldsymbol{n}$ is the unit normal vector pointing from the centre of particle i to that of particle j, and $\boldsymbol{t}$ is the unit tangential vector. If $\boldsymbol{u}_{ij} = \boldsymbol{u}_i - \boldsymbol{u}_j$ denotes the relative velocity between particles then the relative normal velocity can be written as $\boldsymbol{u}_{ij,n} = (\boldsymbol{u}_{ij}\cdot\boldsymbol{n})\boldsymbol{n}$, and the slip velocity at the contact point is

$$\boldsymbol{u}_{ij,t} = \boldsymbol{u}_{ij} - \boldsymbol{u}_{ij,n} + (a_i\boldsymbol{\omega}_i\times\boldsymbol{n} + a_j\boldsymbol{\omega}_j\times\boldsymbol{n}), \tag{3.14}$$

where a denotes the radius of the particle and ω is the rotational velocity of the particle.

The values of k_n and k_t are given using the Hertzian contact theory and Mindlin's theory (Crowe *et al.* 2011)

$$k_n = \frac{4}{3}\left(\frac{1-\sigma_i^2}{E_i} + \frac{1-\sigma_j^2}{E_j}\right)^{-1}\left(\frac{a_i+a_j}{a_ia_j}\right)^{-1/2}, \tag{3.15}$$

$$k_t = 8\left(\frac{2-\sigma_i}{G_i} + \frac{2-\sigma_j}{G_j}\right)^{-1}\left(\frac{a_i+a_j}{a_ia_j}\right)^{-1/2}\delta_n^{1/2}, \tag{3.16}$$

where E and σ are the Young's modulus and Poisson ratio, respectively, and $G = E/2(1+\sigma)$ is the particle shear modulus. Damping coefficients are given as (Barnocky & Davis 1988; Tsuji, Tanaka & Ishida 1992)

$$\eta_n = \phi_n\sqrt{m_pk_n}\delta_n^{1/4}, \quad \eta_t = \phi_t\sqrt{m_pk_t}\delta_t^{1/4}, \tag{3.17a,b}$$

where $m_p = m_im_j/(m_i+m_j)$ is the effective mass, ϕ_n is a constant related to the dry coefficient of restitution e_d as shown in Tsuji *et al.* (1992). If $|\boldsymbol{F}_t| \geq f|\boldsymbol{F}_n|$ then the tangential force is given by the Coulomb-type friction law

$$\boldsymbol{F}_t = -f|\boldsymbol{F}_n|\boldsymbol{t}, \tag{3.18}$$

where f is the friction coefficient. The time step for the collision is set to be one tenth of that for the flow solution (i.e. $\Delta t_c = \Delta t/10$).

Since the DF/FD method is a fixed mesh method, the correction of the lubrication force is needed when two spheres are very close to each other. The lubrication force corrections have the form

$$\boldsymbol{F}_{ij,lub} = -6\pi\mu_f a\boldsymbol{u}_{ij,n}[\lambda(\epsilon) - \lambda(\epsilon_{al})], \tag{3.19}$$

where $\epsilon_{al} = \Delta x/a$ is the threshold gap below which the lubrication correction is activated, where a represents the radius of the particle and Δx is the grid size, and $\lambda(\epsilon)$ is a function of the normalized gap distance $\epsilon = \zeta_n/a$ (Jeffrey 1982), so

$$\lambda(\epsilon) = \frac{1}{4\epsilon} - \frac{9}{40}\ln(\epsilon) - \frac{3}{112}\epsilon\ln(\epsilon) + 0.673 + O(\epsilon). \tag{3.20}$$

Note that the lubrication correction is kept constant for $\epsilon < \epsilon_1$ to account for the lubrication force saturation due to the effect of the surface roughness. In addition, the

https://doi.org/10.1017/jfm.2022.927 Published online by Cambridge University Press

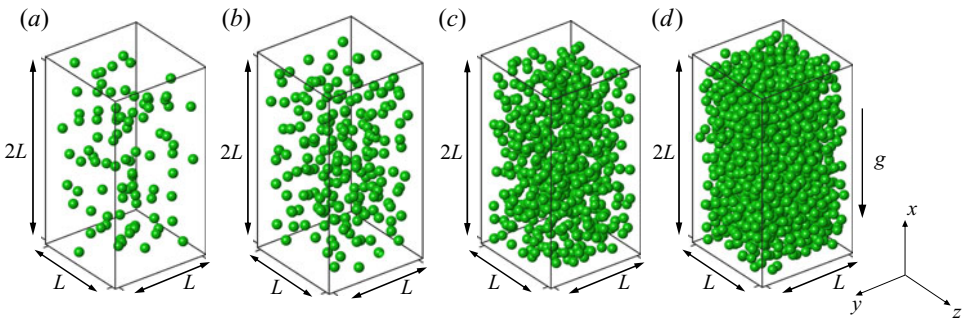


Figure 1. Sketches of the particle sedimentation in a fully periodic domain for three different particle volume fractions: (*a*) $\phi = 2.3\,\%$, (*b*) $\phi = 5.0\,\%$, (*c*) $\phi = 14.2\,\%$, (*d*) $\phi = 30.2\,\%$.

ϕ	2.3 %	5.0 %	14.2 %	30.2 %
N_p	11 / 90	24 / 192	68 / 540	144 / 1152
Ga	24.2–194.0	24.2–218.2	24.2–242.5	24.2–315.2

Table 2. Simulation settings for particles settling in a fully periodic domain at $\rho_r = 2.0$. Here N_p is the total particle number and ϕ is the mean solid volume fraction. Because we have two computational domain sizes, the particle numbers before the '/' correspond to $L/d_p = 5$ while the numbers after the '/' correspond to $L/d_p = 10$.

lubrication force correction is turned off for $\epsilon \leqslant -\epsilon_2$ when two particles overlap and the squeezing fluid film is damaged. Here ϵ_1 and ϵ_2 are set to be 0.001 in our simulations.

3.3. *Simulation set-up*

In the present study we focus on modelling of the interfacial terms for the case where the mean slip velocity exists. Thus, we use the DNS data on the particle sedimentation to establish the correlations for the interfacial terms. As shown in figure 1, the particles are freely settling in a periodic cuboid, with the size of $L_x \times L_y \times L_z = 2L \times L \times L$. The domain is discretized using a uniform Cartesian grid, and the spatial resolution with respect to the particle size is $d_p/\Delta x = 25.6$. The mean velocity of the suspension in the direction of gravity (i.e. x-direction) is kept zero by instantaneously adjusting the pressure gradient.

The parameter settings for our simulations are listed in tables 2 and 3. For convenience, we use ϕ to denote the particle (or solid) volume fraction. The particle number N_p is given by

$$N_p = \left[\frac{6\phi}{\pi} \left(\frac{L}{d_p} \right)^3 \right]. \tag{3.21}$$

We select four solid volume fractions $\phi = 2.3\,\%$, $5.0\,\%$, $14.2\,\%$ and $30.2\,\%$, and two domain sizes: $L/d_p = 5$ and 10 for the liquid–solid case of $\rho_r = 2.0$, as shown in table 2. We also perform some simulations for $\rho_r = 0.01$ and 1000, which represent the bubble–liquid and gas–solid systems, respectively, as shown in table 3. Numerical instability was encountered for $\rho_r = 0.001$ at high particle volume fractions, hence, $\rho_r = 0.001$ is not considered.

https://doi.org/10.1017/jfm.2022.927 Published online by Cambridge University Press

ϕ	N_p	ρ_r	Ga
14.2 %	540	0.01, 1000	24.2, 72.7, 169.7, 242.5
30.2 %	1152	0.01, 1000	24.2, 72.7, 169.7, 315.2

Table 3. Simulation settings used for particles settling in a fully periodic domain of $L/d_p = 10$ for various density ratios.

We take the sphere diameter d_p as the characteristic length, and the characteristic velocity u_c is selected as

$$u_c = \sqrt{\frac{4d_p}{3}(\rho_r - 1)g}. \tag{3.22}$$

The Galileo number is widely used to measure the particle settling effect, which is defined as

$$Ga = \frac{\sqrt{d_p^3(\rho_r - 1)g}}{\nu}. \tag{3.23}$$

The mean relative (or slip) velocity u_r is defined as the difference between the average solid and fluid-phase velocities directed along the x axis as

$$u_r = \langle u_1 \rangle - \langle u_{p,1} \rangle. \tag{3.24}$$

The particle Reynolds number is defined as $Re_p = u_r d_p/\nu$.

We set $E/(\rho_f u_c^2) = 2 \times 10^4$, $\sigma = 0.33$ and $f = 0.3$ for the collision model. The dimensionless time step is $\Delta t = 0.005$ and the statistics are obtained from averaging the data for a duration of 1000 non-dimensional time unit (d_p/u_c) after the statistically steady state is reached. The statistics for the solid-phase velocity and volume fraction are obtained from the data in the solid domain (i.e. inside the particle boundary). Note that we have examined the effects of the box size and the mesh resolution on the results in Appendix A, and ensured that our results are not affected significantly by the box size and the mesh resolution.

4. Modelling of interfacial terms

4.1. *Modelling of dissipation interfacial term*

Using the spatial averaging theorem, Schwarzkopf *et al.* (2009) derived the dissipation rate transport equation of the fluid phase, in which the interfacial terms due to the presence of particles have the form (see also Crowe *et al.* (2011) for the derivation)

$$I_\varepsilon = -\frac{\rho_f \nu^2}{V}\frac{\partial}{\partial x_k}\int_{S_I}\frac{\partial u_i'}{\partial x_j}\frac{\partial u_i'}{\partial x_j}n_k \,\mathrm{d}S + \frac{2\nu}{V}\int_{S_I}\frac{\partial u_i'}{\partial x_j}\frac{\partial p'}{\partial x_j}n_i \,\mathrm{d}S - \frac{\rho_f \nu^2}{V}\int_{S_I}\frac{\partial}{\partial x_k}\left[\frac{\partial u_i'}{\partial x_j}\frac{\partial u_i'}{\partial x_j}\right]n_k \,\mathrm{d}S. \tag{4.1}$$

The first and second terms on the right-hand side of (4.1) are not important, as demonstrated by Schwarzkopf *et al.* (2009). For the Stokes flow in the dilute limit, the

https://doi.org/10.1017/jfm.2022.927 Published online by Cambridge University Press

last term of (4.1) can be simplified as (Schwarzkopf *et al.* 2009; Crowe *et al.* 2011)

$$-\frac{\rho_f \nu^2}{V}\int_{S_I}\frac{\partial}{\partial x_k}\left(\frac{\partial u_i'}{\partial x_j}\frac{\partial u_i'}{\partial x_j}\right)n_k\,\mathrm{d}S = 72\pi\frac{\rho_f\nu^2}{V}\sum_k\frac{(\langle u_i\rangle - u_{pki})^2}{d_p} = 24\frac{\nu}{d_p^2}I_k. \tag{4.2}$$

The constant '24' can be replaced by the so-called dissipation interfacial term coefficient $C_{\varepsilon 3}$ to account for non-Stokesian effects, resulting in

$$I_\varepsilon = C_{\varepsilon 3}\frac{\nu}{d_p^2}I_k. \tag{4.3}$$

Accurate computation of the interfacial term via the integration of (4.2) on the particle surface is difficult for the non-body-fitted approach. Therefore, we quantify it by considering the dissipation rate balance equation (Schwarzkopf *et al.* 2009). For the fully developed homogeneous system with $\mathrm{d}k/\mathrm{d}t = 0$, $\mathrm{d}\varepsilon/\mathrm{d}t = 0$ and $\partial\langle\cdot\rangle/\partial x_i = 0$, the k and ε equations reduce to

$$I_k = \phi_f\rho_f\varepsilon, \tag{4.4}$$

$$I_\varepsilon = C_{\varepsilon 2}\phi_f\rho_f\frac{\varepsilon^2}{k}. \tag{4.5}$$

From (4.3)–(4.5), we have

$$\frac{C_{\varepsilon 3}}{C_{\varepsilon 2}} = \frac{d_p^2}{\nu}\frac{\varepsilon}{k}. \tag{4.6}$$

From (2.21) and (4.4), one can obtain

$$\varepsilon = \frac{F_D u_r}{\phi_f\rho_f}. \tag{4.7}$$

Substituting (4.7) into (4.6) yields

$$\frac{C_{\varepsilon 3}}{C_{\varepsilon 2}} = \frac{d_p^2}{\nu}\frac{1}{\phi_f\rho_f k}F_D u_r = Re_p\frac{d_p F_D}{(1-\phi)\rho_f(k/u_r^2)u_r^2}, \tag{4.8}$$

which indicates that $C_{\varepsilon 3}/C_{\varepsilon 2}$ is related to the relative TKE k/u_r^2 and the mean drag force F_D. Hence, to model the interfacial term in the dissipation rate equation, the correlations for the mean drag and the relative TKE are required.

Based on interface-resolved simulations of the flow past fixed random assemblies of monodisperse spheres ($0.1 \le \phi \le 0.5$, $0.01 \le Re_m \le 300$, where $Re_m = (1-\phi)Re_p$), Mehrabadi *et al.* (2015) proposed the following correlation for the particle-induced relative TKE:

$$\frac{k}{u_r^2} = \phi + 1.25\phi(1-\phi)^3\exp(-\phi Re_m^{1/2}). \tag{4.9}$$

This was shown to be applicable to the dynamic sedimentation system. In the present work we attempt to quantify the relative TKE for the dynamic sedimentation system at different density ratios. Figure 2(*a*) shows the variation of k/u_r^2 with the particle Reynolds number for different solid volume fractions at a density ratio of 2. k/u_r^2 for two different box sizes of $L/d_p = 10$ and 5, which shows that k/u_r^2 slightly increases with increasing domain size. Figure 2(*b*) shows the effects of the density ratio on k/u_r^2 for $\phi = 14.2\,\%$

https://doi.org/10.1017/jfm.2022.927 Published online by Cambridge University Press

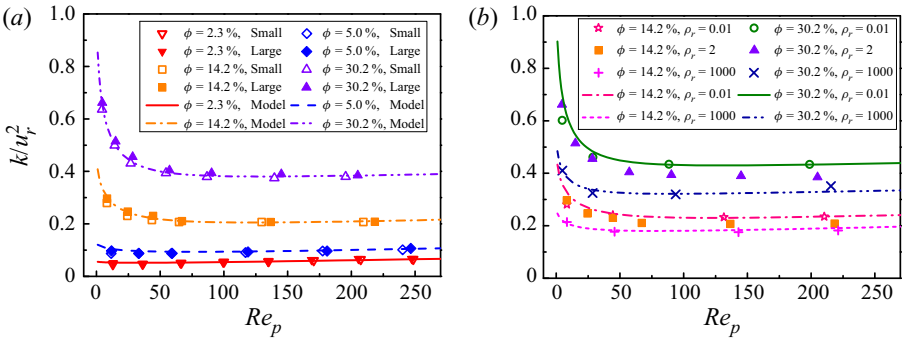


Figure 2. Relative TKE k/u_r^2 as a function of Re_p for (*a*) $\rho_r = 2.0$ and different domain sizes, and (*b*) $\rho_r = 0.01$ and 1000 at $L/d_p = 10$. The symbols represent the IR-DNS data, while the lines denote the corresponding correlations (4.10). In the legend of (*a*), 'small' represents the smaller domain of $L/d_p = 5$, while 'large' represents the larger domain of $L/d_p = 10$.

and 30.2 %. From figure 2(*a*), k/u_r^2 decreases rapidly with increasing particle Reynolds number at relatively small Re_p, particularly for dense suspensions, consistent with previous simulations of Mehrabadi *et al.* (2015). For dilute suspensions, we observe a slight increase in k/u_r^2 with increasing Re_p at $Re_p > 100$. From figure 2(*b*), k/u_r^2 is higher for a lower density ratio. Using the present DNS data ($0.023 \leq \phi \leq 0.302$, $Re_p \leq 250$) and inspired by the correlation function form of Mehrabadi *et al.* (2015), a correlation for the relative TKE is obtained as

$$\frac{k}{u_r^2} = 0.92\rho_r^{-0.02}\phi^{0.78} + 0.05\phi^{0.3}(1-\phi)(Re_p/200)^{1.1} + 25\phi^2(\rho_r + 0.5)^{-0.15}(1-\phi)^3 \exp(-\phi^{1/2}(1-\phi)^{1/2}Re_p{}^{1/2}). \tag{4.10}$$

Figure 2 shows that the above correlation agrees well with our DNS data. Figure 3 compares the present correlation of the relative TKE for $\rho_r = 1000$ to that of Mehrabadi *et al.* (2015) obtained from the simulations of fixed spheres. Both correlations are in fairly good agreement with each other. One discrepancy is that the relative TKE of Mehrabadi *et al.* (2015) decreases monotonically with increasing Re_p, whereas ours slightly increases with increasing Re_p for $Re_p > 100$. Mehrabadi *et al.* (2015) observed that the relative TKE for freely moving particles was slightly greater than that for fixed particles at relatively high Re_p. Our computational domain size is larger than that of Mehrabadi *et al.* (2015), and it has been observed that the relative TKE increases with increasing domain size. Therefore, the differences in the domain size and particle mobility may be responsible for the above discrepancy.

We now intend to establish the correlation for the mean drag from our DNS data, which is also required for modelling the dissipation interfacial term (4.8). We take the following form for the drag correlation

$$F_D = \beta u_r, \tag{4.11}$$

where β is the momentum transfer coefficient.

For $\phi \leq 0.1$, we adopt the correlation of β obtained in our previous work (Xia *et al.* 2022*b*),

$$\beta_1 = \frac{3}{4}C_d\frac{\rho_f\phi(1-\phi)u_r}{d_p}(1-\phi)^{-n}, \tag{4.12}$$

https://doi.org/10.1017/jfm.2022.927 Published online by Cambridge University Press

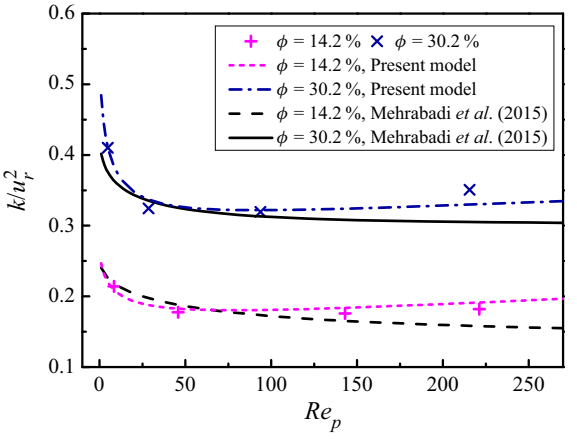


Figure 3. Comparison of relative TKE k/u_r^2 obtained from the present simulations and from the correlation of Mehrabadi *et al.* (2015). Our IR-DNS data for $\rho_r = 1000$, denoted by the symbols, and our correlation (4.10), denoted by the lines, are both shown.

where C_d is the modified drag coefficient

$$C_d = \frac{24}{(1-\phi)Re_p}(1 + 0.15((1-\phi)Re_p)^{0.687}), \tag{4.13}$$

and n is the exponent of the correction function in the form

$$n = (3.88 - 0.38\ln(Re_p))\ln(\phi^{-1})\rho_r^{-0.038}. \tag{4.14}$$

For $\phi > 0.1$, based on our DNS data and the modification of the drag correlation of Tang *et al.* (2015) by considering the effects of particle mobility and density ratio, we obtain the following drag correlation:

$$\begin{aligned}\beta_2 = {} & 180\frac{\mu\phi^2}{d_p^2(1-\phi)} + 18\frac{\mu(1-\phi)^3\phi(1+1.5\sqrt{\phi})}{d_p^2} + \frac{18\mu\phi(1-\phi)Re_m}{d_p^2}\left[0.11\phi(1+\phi)\right. \\ & \left. - \frac{0.00456}{(1-\phi)^4} + \left(0.169(1-\phi) + \frac{0.0644}{(1-\phi)^4}\right)Re_m^{-0.343}\right] \\ & + 2.76Re_m^{0.8}\rho_r^{-0.05}\frac{\mu\phi^2}{d_p^2(1-\phi)}.\end{aligned} \tag{4.15}$$

We note that in order to avoid the discontinuity of β at the critical solid volume fraction (e.g. 0.1 here), Lu *et al.* (2003) proposed a continuous stitching function as $\beta = \kappa\beta_1 + (1-\kappa)\beta_2$, with $\kappa = \arctan[150 \times 1.75(0.1-\phi)]/\pi + 0.5$ being an inverse tangent function.

The mean drag forces F_D obtained from IR-DNS normalized with $3\pi\mu(1-\phi)d_p u_r/d_p^3$ at different Re_p and ϕ are compared with the present drag correlations in figure 4. The correlations agree well with our DNS data for all cases considered, as shown in figure 4.

https://doi.org/10.1017/jfm.2022.927 Published online by Cambridge University Press

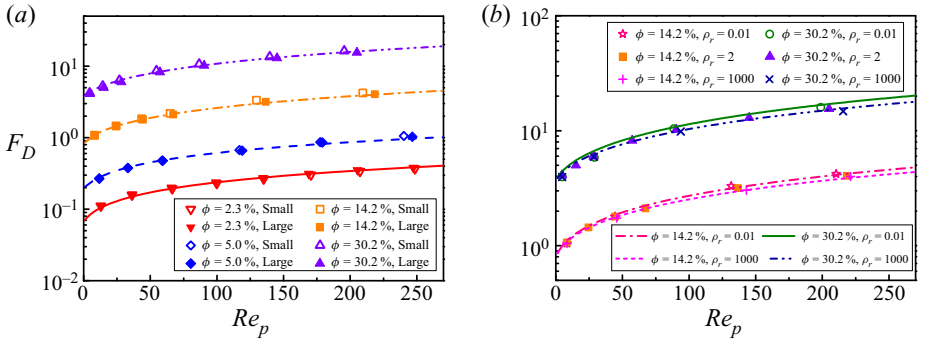


Figure 4. Mean drag forces F_D, normalized with $3\pi\mu(1-\phi)d_p u_r/d_p^3$, as a function of Re_p for different ϕ, and (*a*) $\rho_r = 2.0$, (*b*) $\rho_r = 0.01$–1000 and $L/d_p = 10$. The symbols denote the IR-DNS data, while the lines present the corresponding drag correlation (4.12) or (4.15). In the legend of (*a*) , 'small' represents the smaller domain of $L/d_p = 5$, while 'large' represents the larger domain of $L/d_p = 10$.

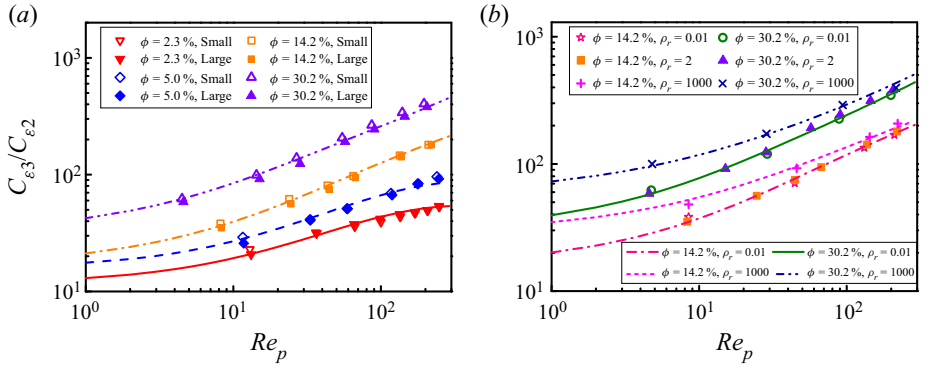


Figure 5. Coefficient ratio $C_{\varepsilon 3}/C_{\varepsilon 2}$ as a function of Re_p at different solid volume fractions and (*a*) $\rho_r = 2.0$, (*b*) $\rho_r = 0.01$ and 1000, and $L/d_p = 10$. The symbols denote the IR-DNS data, while the lines denote the correlation (4.16).

With the established correlations for the relative TKE (4.10) and the mean drag coefficient (4.11), the ratio $C_{\varepsilon 3}/C_{\varepsilon 2}$ can be modelled as

$$\frac{C_{\varepsilon 3}}{C_{\varepsilon 2}} = \frac{\beta Re_p}{\rho_f(1-\phi)(k/u_r^2)}\frac{d_p}{u_r}. \tag{4.16}$$

The comparison of this correlation with the IR-DNS data is shown in figure 5. From figure 5(*a*), $C_{\varepsilon 3}/C_{\varepsilon 2}$ increases with increasing particle Reynolds number or solid volume fraction, when the other parameters are fixed. In addition, the effect of the computational domain size becomes more pronounced at a higher solid volume fraction, and $C_{\varepsilon 3}/C_{\varepsilon 2}$ is larger for a smaller domain size. Figure 5(*b*) shows that $C_{\varepsilon 3}/C_{\varepsilon 2}$ is much higher for $\rho_r = 1000$ than those for $\rho_r = 2$ and 0.01, which indicates that the dissipation rate interfacial term is higher for particles with a larger density at the same particle Reynolds number and solid volume fraction.

In the dilute limit, $C_{\varepsilon 3}$ can be simplified as

$$C_{\varepsilon 3} = \frac{3}{4}C_{\varepsilon 2}\frac{\phi}{k/u_r^2}C_D Re_p. \tag{4.17}$$

https://doi.org/10.1017/jfm.2022.927 Published online by Cambridge University Press

Reference	Carrier	Disperse	Re_b	Re_p	$d_p/2H$	ρ_r	ϕ_0
Santarelli & Fröhlich (2015), Santarelli *et al.* (2016)	Water	Bubbles	5263	236–475	0.052–0.076	0.01	0.0029–0.0214
Uhlmann (2008)	Water	Solid particles	5400	136	0.05	2.21 or 10	0.0042
Yu *et al.* (2021)	Water	Solid particles	5746, 12 000	50–225	0.05, 0.1	2.0–100	0.0236

Table 4. Summary of the previous works on interface-resolved simulations of vertical turbulent particle-laden channel flows.

Therefore, the interfacial term of dissipation rate I_ε can be expressed as

$$I_\varepsilon = \frac{3}{4} C_{\varepsilon 2} \frac{\phi}{k/u_r^2} C_D Re_p \frac{\nu}{d_p^2} I_k = \frac{3}{4} C_{\varepsilon 2} \frac{\phi}{k/u_r^2} C_D \frac{I_k}{\tau}, \tag{4.18}$$

where $\tau = d_p/u_r$. Our model in the dilute limit (4.18) has a form similar to that of Troshko & Hassan (2001) ($I_\varepsilon = 1.35 C_D I_k/\tau$) and Ma *et al.* (2017)($I_\varepsilon = 0.3 C_D I_k/\tau$), as shown in table 1.

From (4.8), we have

$$\left[(1-\phi)(k/u_r^2)\frac{C_{\varepsilon 3}}{C_{\varepsilon 2}}\right] \Big/ \left[\frac{d_p F_D}{\rho_f u_r^2}\right] = Re_p. \tag{4.19}$$

We collect the IR-DNS data on vertical channel flows laden with bubbles or heavy particles in the literature (Uhlmann 2008; Santarelli & Fröhlich 2015; Santarelli *et al.* 2016; Yu *et al.* 2021), as summarized in table 4, and compare them with our model in figure 6. It is noted that the values of $C_{\varepsilon 3}/C_{\varepsilon 2}$ in figure 6 are calculated directly from (4.6), and F_D and k/u_r^2 are computed with our correlations (4.10) and (4.11). All data are collected in the sedimentation-dominated regime of $\sqrt{k}/u_r \ll 1$ at the channel centre. Our model agrees very well with the DNS data of Yu *et al.* (2021) for particle Reynolds numbers below 200, and is in fairly good agreement with those of Uhlmann (2008), Santarelli & Fröhlich (2015) and Santarelli *et al.* (2016).

4.2. *Modelling of the interfacial term in Reynolds stress equation*

The presence of particles gives rise to strong anisotropy for the Reynolds stress transport. For the homogeneous sedimentation system at steady state, the Reynolds stress equations (2.4) reduce to

$$\Phi_{ij} - \varepsilon_{ij} + I_{ij} = 0. \tag{4.20}$$

Considerable efforts have been devoted to the modelling of the dissipation rate tensor ε_{ij}, pressure–strain term Φ_{ij} and interfacial term I_{ij}.

Poelma, Westerweel & Ooms (2007) have demonstrated experimentally that relative motion between the phases induced by gravity forces can lead to significant anisotropy in the fluid-phase dissipation tensor ε_{ij}. Using the present DNS data, we determine the coefficient f_s in (2.8), and the results for different Re_p and ϕ at $\rho_r = 2.0$ are plotted in figure 7(*a*). Baker *et al.* (2020) adopted $f_s = 0.9$. Figure 7(*a*) shows that f_s from our DNS data is insensitive to the variation of Re_p and ϕ, and $f_s = 0.9$ is a good choice.

https://doi.org/10.1017/jfm.2022.927 Published online by Cambridge University Press

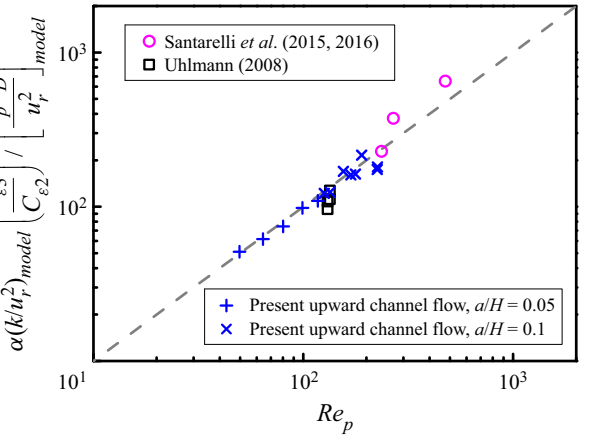


Figure 6. Previous IR-DNS data on $C_{\varepsilon 3}/C_{\varepsilon 2}$ at the channel centre for vertical channel flows, as compared with the model (4.19).

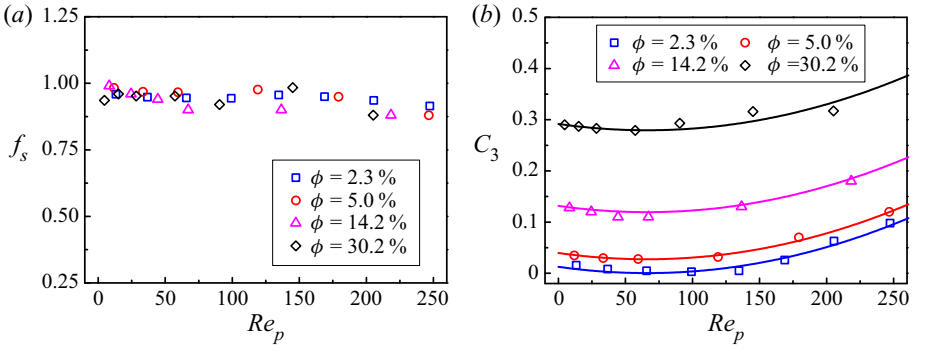


Figure 7. Plots of (*a*) f_s and (*b*) C_3 as a function of Re_p for different solid volume fractions and $\rho_r = 2$. The symbols denote our IR-DNS data, and the solid lines represent the model (4.22).

It should be noted that the results for $\rho_r = 0.01$ and 1000 are similar to those for $\rho_r = 2.0$ in figure 7(*a*), but are not shown here for clarity.

For the homogeneous sedimentation system, the pressure–strain term Φ_{ij} reduces to

$$\Phi_{ij} = -\phi_f \rho_f C_1 \varepsilon a_{ij} + \phi_f \rho_f C_1' \varepsilon (a_{ik}a_{kj} - \tfrac{1}{3}A_2\delta_{ij}) - C_3(I_{ij} - \tfrac{1}{3}\delta_{ij}I_{kk}). \tag{4.21}$$

With the standard coefficients $C_1 = 1.7$ and $C_1' = 1.05$ for the SSG model (Hanjalić & Launder 2011), the only unknown coefficient C_3 can be obtained using the DNS data from (4.21). The results are shown in figure 7(*b*). Obviously, C_3 increases with increasing ϕ. For dilute flows ($\phi = 2.3\,\%$) at $Re_p < 150$, C_3 is almost zero. For $\rho_r = 2$, C_3 is a function of particle volume fraction and particle Reynolds number in the form

$$C_3(\phi, Re_p) = \phi + aRe_p + bRe_p^2 + c, \tag{4.22}$$

in which $a = 3.723 \times 10^{-4}$, $b = 2.819 \times 10^{-6}$ and $c = -0.010$. The correlation of C_3 (4.22) is compared with the DNS data in figure 7(*b*), and good agreement can be observed. We note that C_3 is not sensitive to the variation of the density ratio from our DNS (not shown here), thus, the correlation (4.22) is applicable to other density ratios.

https://doi.org/10.1017/jfm.2022.927 Published online by Cambridge University Press

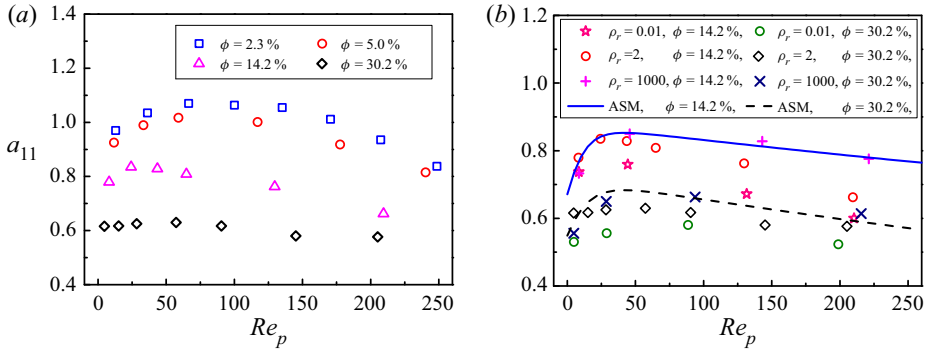


Figure 8. Reynolds stress anisotropy component a_{11} for different Re_p and ϕ at (*a*) $\rho_r = 2.0$ and (*b*) $\rho_r =$ 0.01–1000. The symbols denote our IR-DNS data, while the lines represent the model proposed by Mehrabadi *et al.* (2015) from DNS of fixed particles.

The non-monotonic trend of C_3 with Re_p may be related to the particle-induced fluid Reynolds stress anisotropy a_{ij} defined by (2.14), since C_3 is determined from (4.21) with the DNS data of a_{ij}, Φ_{ij} and I_{ij}. Our results on the Reynolds stress anisotropy component in the vertical direction a_{11} are shown in figure 8. From figure 8, a_{11} increases with increasing Re_p at relatively low Re_p, and then decreases with increasing Re_p above a critical Re_p, being opposite to the dependence of C_3 on Re_p, as shown in figure 7(*b*). From figure 8, a_{11} decreases with increasing ϕ, which indicates that the anisotropy of the velocity fluctuation decreases with increasing ϕ, since $a_{11} + a_{22} + a_{33} = 2$ and $a_{22} = a_{33}$. Mehrabadi *et al.* (2015) argued that the magnitude of anisotropy is determined by the ratio of the length of elongated structures to the inter-particle spacing (Mehrabadi *et al.* 2015). In addition, figure 8(*b*) shows that a_{11} increases with increasing density ratio, particularly for high Re_p, and a_{11} for $\rho_r = 1000$ is in good agreement with the algebraic stress model proposed by Mehrabadi *et al.* (2015) obtained from the DNS data for fixed spheres, which provides evidence for good accuracy of our DNS data.

The force term $\Phi_{ij,3}$ with the coefficient of C_3 in the pressure–strain model is caused by the presence of particles, and this term can be combined with the interfacial term I_{ij}. Ma *et al.* (2020*b*) defined an effective particle-induced interfacial term $I^*_{ij} = \Phi_{ij,3} + I_{ij}$, i.e.

$$I^*_{ij} = b_{ij} I_k - C_3 (I_{ij} - \tfrac{1}{3}\delta_{ij} I_{kk}) = [(1 - C_3) b_{ij} + \tfrac{2}{3} C_3 \delta_{ij}] I_k. \tag{4.23}$$

Therefore, we have $I^*_{ij} = b^*_{ij} I_k$, with

$$b^*_{ij} = (1 - C_3) b_{ij} + \tfrac{2}{3} C_3 \delta_{ij}. \tag{4.24}$$

As discussed in § 2, $b_{11} = 2.0$ and $b_{22} = b_{33} = 0$, if the mean slip velocity exists only in one direction. Figure 9 shows b^*_{11} as a function of Re_p for different ϕ at $\rho_r = 2$. Clearly, b^*_{11} decreases with increasing ϕ, as a_{11} in figure 8, which indicates a trend towards stronger isotropy at a higher ϕ. For $\phi = 2.3\,\%$ and $Re_p < 150$, our b^*_{11} is close to 2.0, which is consistent with the correlation of Ma *et al.* (2020*b*) from DNS of bubbly flows at relatively low particle volume fractions and high particle Reynolds numbers: $b^*_{11} = \min(0.67 + 0.67 \exp(370 Re_p^{-1.2}), 2)$ (Ma *et al.* 2020*b*).

5. Reynolds-averaged simulation of turbulent channel flows

It remains unclear whether the existing multiphase turbulence models can correctly predict the turbulence enhancement or attenuation induced by particles. In this section

https://doi.org/10.1017/jfm.2022.927 Published online by Cambridge University Press

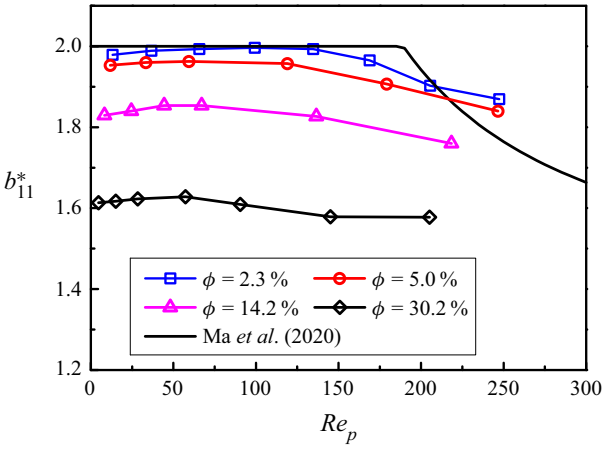


Figure 9. Modified interfacial term b_{11}^* as a function of Re_p for different ϕ at $\rho_r = 2$. The solid line represents the correlation of Ma *et al.* (2020*b*).

Case	ρ_r	$d_p/2H$	ϕ_0	Ga	Re_p	Re_b	Flow direction	Source
1	2.0	0.05	2.36 %	22.9	9.5	5746	Upward	Yu
2	2.0	0.05	2.36 %	62.2	49.6	5746	Upward	Yu
3	2.0	0.05	2.36 %	112.0	113.5	5746	Upward	Yu
4	2.0	0.05	2.36 %	103.9	102.1	12000	Upward	Yu
5	2.0	0.05	2.36 %	49.8	38.3	5746	Downward	Xia
6	100	0.05	2.36 %	112.0	90.6	5746	Downward	Xia
7	2.21	0.025	0.42 %	115.5	130.5	5400	Upward	Uhlmann
8	0.001	0.052	2.14 %	195.4	235.5	5263	Upward	Santarelli
9	2.0	0.05	14.2 %	50.0	22.9	5746	Upward	Present work

Table 5. Key parameters for the selected particle-laden flows in a vertical channel (Uhlmann 2008; Santarelli *et al.* 2016; Xia *et al.* 2021; Yu *et al.* 2021). Here ϕ_0 is the mean solid volume fraction in the entire channel, $Re_b = u_b(2H)/\nu$ is the bulk Reynolds number, Re_p is the particle Reynolds number based on the mean interphase slip velocity at the channel centre.

the particle-laden flows in a vertical channel at relatively low particle volume fractions are simulated using the RSM with the interfacial term correlations developed in the present study. The results are compared with the IR-DNS data of Yu *et al.* (2021), Xia *et al.* (2021), Uhlmann (2008) and Santarelli *et al.* (2016) (see table 5 for the parameter settings), in order to validate our new models. In addition, a new IR-DNS simulation with a particle volume fraction of 14.2 % (case 9 in table 5) is performed in the present work to validate the accuracy of our model for relatively large volume fractions.

5.1. *Near-wall RSM for particle-laden turbulent channel flows*

Most turbulence models were developed for high Reynolds numbers, and they are not suitable for low-*Re* wall-bounded channel flows where the viscous effects permeate the whole region. The Reynolds numbers for all IR-DNS data available are low, hence, the near-wall Reynolds stress model (So *et al.* 1996) for the single-phase turbulent flows is employed. In the present study we assume that the presence of particles do not affect

https://doi.org/10.1017/jfm.2022.927 Published online by Cambridge University Press

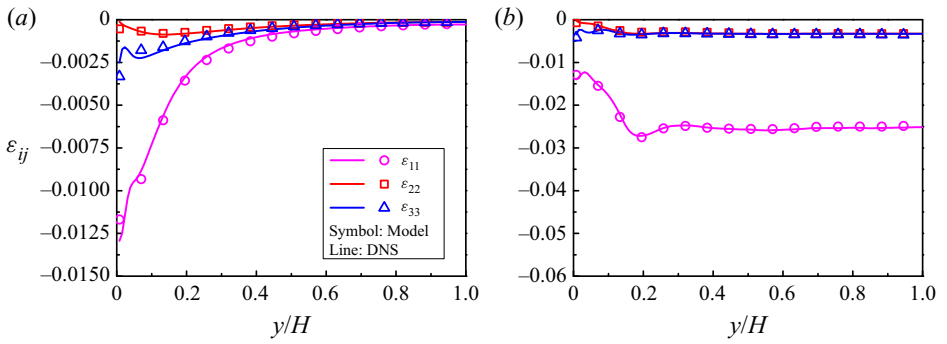


Figure 10. Comparison between the dissipation rate tensor ε_{ij} obtained fully from the DNS simulations and from the model (2.8) with $f_s = 0.9$ and the DNS data of the dissipation rate ε for (*a*) case 1 ($Re_p = 9.5$) and (*b*) case 3 ($Re_p = 113.5$). All values are normalized with $\rho_f u_b^3/H$.

the model parameters existing in the single-phase case in (2.4) and (2.23), and we only supplement with the particle-induced terms.

For the dissipation term, the model (2.8) is employed with $f_s = 0.9$, as discussed earlier in association with figure 7(*a*). The components of the dissipation term ε_{ij} predicted by the model (2.8) using the DNS data of the dissipation rate ε and Reynolds stresses are compared with the DNS data of ε_{ij} for the typical cases (cases 1 and 3) in figure 10. Remarkably good agreement can be seen, which indicates that the anisotropic model (2.8) with $f_s = 0.9$ is suitable for the particle-laden channel flow.

From (2.10)–(2.13), the pressure–strain tensor Φ_{ij} for turbulent channel flows reads

$$\begin{aligned}\Phi_{ij} = &-\phi_f\rho_f(C_1\varepsilon + C_1^* P_k)a_{ij} + \phi_f\rho_f C_1'\varepsilon(a_{ik}a_{kj} - \tfrac{1}{3}A_2\delta_{ij})\\ &- \phi_f\rho_f C_2(P_{ij} - \tfrac{2}{3}P_k\delta_{ij}) - \phi_f\rho_f C_4(E_{ij} - \tfrac{2}{3}P_k\delta_{ij})\\ &- \phi_f\rho_f(0.033 + 0.65A_2^{1/2})kS_{ij} - C_3(I_{ij} - \tfrac{1}{3}\delta_{ij}I_{kk}) + \Phi_{ij}^w. \end{aligned} \tag{5.1}$$

Here the near-wall correction tensor Φ_{ij}^w is given by So *et al.* (1996)

$$\Phi_{ij}^w = f_w\phi_f\rho_f[(C_1\varepsilon + C_1^* P_k)a_{ij} - C_1'\varepsilon(a_{ik}a_{kj} - \tfrac{1}{3}A_2\delta_{ij}) + \alpha^*(P_{ij} - \tfrac{2}{3}P_k\delta_{ij}) + 2\gamma^* kS_{ij}], \tag{5.2}$$

where f_w is a damping function given as $f_w = \exp[-(\mathrm{Re}_t/200)^2]$, with Re_t being the turbulent Reynolds number $Re_t = k^2/\varepsilon\nu$. Here α^* and γ^* are constants in the SSG model, which can provide a better prediction for a fully developed channel flow in the near-wall region.

Comparison between the pressure–strain terms obtained directly from (2.9) and from the model (5.1) using the DNS data for cases 1 and 3 is shown in figure 11. The model predicts well the pressure–strain term for both shear-induced turbulence and particle-induced turbulence in the bulk region, but the accuracy of the model is not good in the near-wall region. It is a difficult issue how to accurately model the pressure–strain term in the near-wall region for low-*Re* wall-bounded flows even for the single-phase case.

In the modelled ε equation, to account for near-wall effects, the term ε_ε is modified as

$$\varepsilon_\varepsilon = C_{\varepsilon 2}\phi_f\rho_f\frac{\varepsilon\tilde{\varepsilon}}{k}, \tag{5.3}$$

https://doi.org/10.1017/jfm.2022.927 Published online by Cambridge University Press

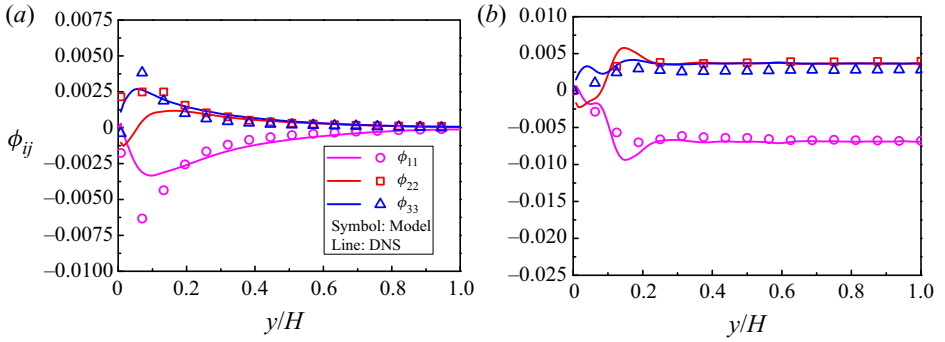


Figure 11. Comparison between the pressure–strain terms Φ_{ij} obtained directly from (2.9) and from the model (5.1) using the DNS data for (*a*) ($Re_p = 9.5$) and (*b*) case 3 ($Re_p = 113.5$). All values are normalized with $\rho_f u_b^3/H$.

where $\tilde{\varepsilon} = \varepsilon - 2\nu(\sqrt{k}/y)^2$, with y being the normal distance from the wall. The difference between $\tilde{\varepsilon}$ and ε disappears at the edge of the viscous region for the low-Reynolds-number case (e.g. $Re_\tau = 180$) (Hanjalić & Launder 2011).

5.2. *Comparison between RANS and DNS*

We consider vertical channel flows, with gravity points downwards. We define the streamwise, wall-normal and spanwise directions as x, y and z, respectively, and also as x_1, x_2 and x_3, respectively. For fully developed channel flows, we have $\langle u_3' u_1' \rangle = \langle u_3' u_2' \rangle = 0$, $\langle u_2 \rangle = \langle u_3 \rangle = 0$ and $\partial \langle u_1 \rangle / \partial x_1 = \partial \langle u_1 \rangle / \partial x_3 = 0$. Thus, the dimensionless volume-averaged equations for the fluid phase can be simplified as

$$\left.\begin{aligned}
\frac{\partial \phi_f \langle u_1 \rangle}{\partial t} &= -\phi_f \frac{\mathrm{d}\langle p \rangle}{\mathrm{d}x_1} + \frac{1}{Re}\frac{\partial}{\partial x_2}\left(\phi_f \frac{\partial \langle u_1 \rangle}{\partial x_2}\right) - \frac{\partial(\phi_f \langle u_1' u_2' \rangle)}{\partial x_2} - F_D, \\
\frac{\partial \phi_f \langle u_1' u_1' \rangle}{\partial t} &= -2\phi_f \langle u_1' u_2' \rangle \frac{\partial \langle u_1 \rangle}{\partial x_2} + D_{11} + \Phi_{11} + \varepsilon_{11} + I_{11}, \\
\frac{\partial \phi_f \langle u_2' u_2' \rangle}{\partial t} &= D_{22} + \Phi_{22} + \varepsilon_{22} + I_{22}, \\
\frac{\partial \phi_f \langle u_3' u_3' \rangle}{\partial t} &= D_{33} + \Phi_{33} + \varepsilon_{33} + I_{33}, \\
\frac{\partial \phi_f \langle u_1' u_2' \rangle}{\partial t} &= -\phi_f \langle u_2' u_2' \rangle \frac{\partial \langle u_1 \rangle}{\partial x_2} + D_{12} + \Phi_{12} + \varepsilon_{12} + I_{12}, \\
\frac{\partial \phi_f \varepsilon}{\partial t} &= P_\varepsilon + D_\varepsilon + \varepsilon_\varepsilon + I_\varepsilon.
\end{aligned}\right\} \tag{5.4}$$

The pressure gradient is determined from the constraint that the flow rate (or bulk velocity) is constant. The following boundary conditions are imposed on the wall: $\langle u_i \rangle = 0$, $\langle u_i' u_j' \rangle = 0$ and $\varepsilon = 2\nu(\mathrm{d}\sqrt{k}/\mathrm{d}x_2)^2$. Equations (5.4) are solved with an in-house code using a time advancement scheme to achieve the steady-state solution.

The full two-fluid RSM is complex (Fox 2014; Baker *et al.* 2020), involving some sub-models for the solid phase, such as the lift model and the particle stress model. In order to evaluate the performance of the interfacial term models proposed in the present study, the uncertainty from other models should be minimized. Therefore, inspired by the work of Ma *et al.* (2020*b*), we only solve the fluid-phase transport equations (5.4), and

https://doi.org/10.1017/jfm.2022.927 Published online by Cambridge University Press

c_s	C_1	C_1'	C_2	C_3	C_1^*	C_4	α^*	γ^*	$C_{\varepsilon 1}$	$C_{\varepsilon 2}$	σ_ε	f_s
0.22	1.7	1.05	0.4125	0.0	0.45	0.2125	−0.29	0.065	1.44	1.83	1.36	0.9

Table 6. Coefficients in the present RANS simulations of particle-laden channel flows.

directly use the DNS data for the solid-phase quantities involved in the fluid equations, such as the particle volume fraction, the mean slip velocity and the mean drag. Table 6 presents the empirical coefficients in our RANS simulations.

The DNS mean drag is obtained from the fluid mean momentum equation in the dimensional form at statistically steady state

$$F_D = \frac{\mathrm{d}}{\mathrm{d}x_2}\left(\phi_f \mu \frac{\mathrm{d}\langle u_1\rangle}{\mathrm{d}x_2}\right) + \phi_f\left(-\frac{\mathrm{d}p_e}{\mathrm{d}x_1}\right) + \frac{\mathrm{d}}{\mathrm{d}x_2}(\phi_f \rho_f \langle -u_1' u_2'\rangle). \tag{5.5}$$

From the domain-averaged momentum balance for the mixture, the mean pressure gradient $-\mathrm{d}p_e/\mathrm{d}x = \tau_w/H + \phi_0(\rho_s - \rho_f)g$ for upward flow, while $-\mathrm{d}p_e/\mathrm{d}x = \tau_w/H - \phi_0(\rho_s - \rho_f)g$ for downward flow.

To evaluate the performance of the original near-wall RSM for the single-phase flow, we compare the results on the single-phase turbulent channel flow from the model with the DNS results of Hoyas & Jiménez (2008) in Appendix B. It is shown that the model can predict well the turbulence statistics, which lays a foundation for the application of the RSM to particle-laden flows.

The results on TKE from the RANS simulations of upward particle-laden turbulent channel flows for cases 1–3 in table 5 are compared with the DNS results of Yu *et al.* (2021) in figure 12. Turbulence suppression across the entire channel is observed for cases 1 ($Re_p = 9.5$) and 2 ($Re_p = 49.6$), whereas turbulence augmentation in the bulk region takes place for case 3 ($Re_p = 113.5$). The RANS results agree well with the DNS results, as shown in figure 12. To the best of our knowledge, this is the first demonstration of using RANS simulations to well predict particle-induced turbulence enhancement and attenuation in vertical channel flows.

Figures 13 and 14 show that the root-mean-square (r.m.s.) values of the fluid velocity fluctuations and some selected terms in the Reynolds stress equation of $\langle u_1' u_1'\rangle$ from RANS agree well with the DNS results, which indicate that the particle-induced anisotropy is correctly captured by our RSM. Nevertheless, significant over-estimation of v'_{rms} and w'_{rms} near the wall by the RANS simulations can be observed in figure 13(*a*). We note that such over-prediction occurs for the RANS simulation of the single-phase flow, as shown in figure 22. In addition, figure 13 shows that the discrepancy of wall-normal and spanwise r.m.s. velocities between Euler–Euler RANS and IR-DNS becomes relatively larger in the centre region of the channel at a higher particle Reynolds number, which is a surprising result, since one may assume that the flow tends to become a more homogeneous sedimentation system as the particle Reynolds number increases. From our previous study (Yu *et al.* 2021), the shear turbulence (characterized by the Reynolds shear stress) in an upward channel flow can be attenuated by the settling particles, however, the effect is non-monotonic with increasing particle Reynolds number. Above the critical Re_p, the Reynolds shear stress increases with increasing Re_p (see also figure 16), which may indicate that the flow deviates more from the homogeneous sedimentation system at a higher Re_p. Our models for the interfacial terms are based on the data of the homogeneous sedimentation in a periodic domain, and we conjecture that this is the reason why the

https://doi.org/10.1017/jfm.2022.927 Published online by Cambridge University Press

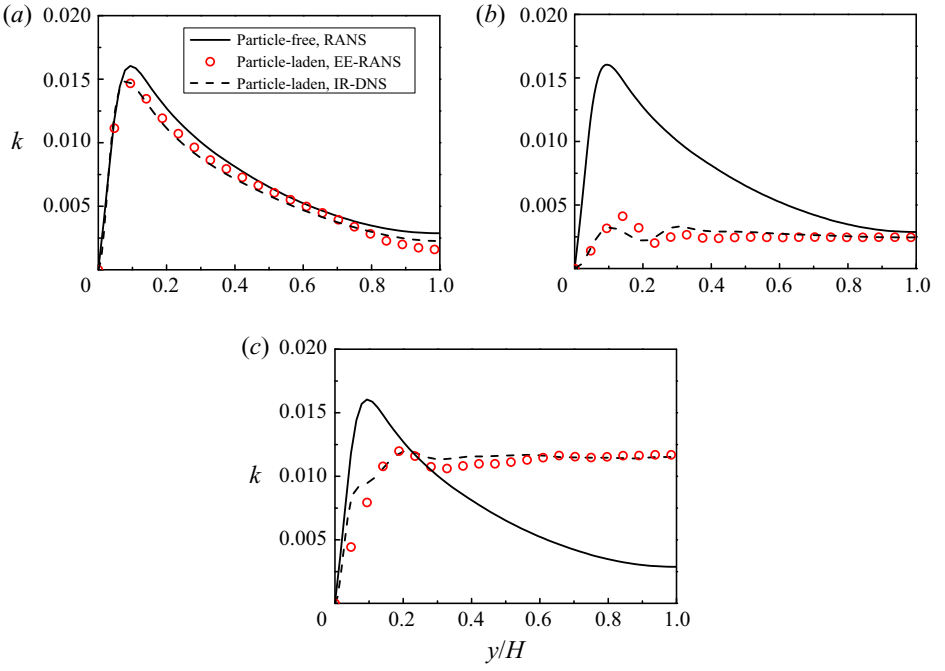


Figure 12. Profiles of TKE for (*a*) case 1 (upflow, $Re_p = 9.5$), (*b*) case 2 (upflow, $Re_p = 49.6$), (*c*) case 3 (upflow, $Re_p = 113.5$).

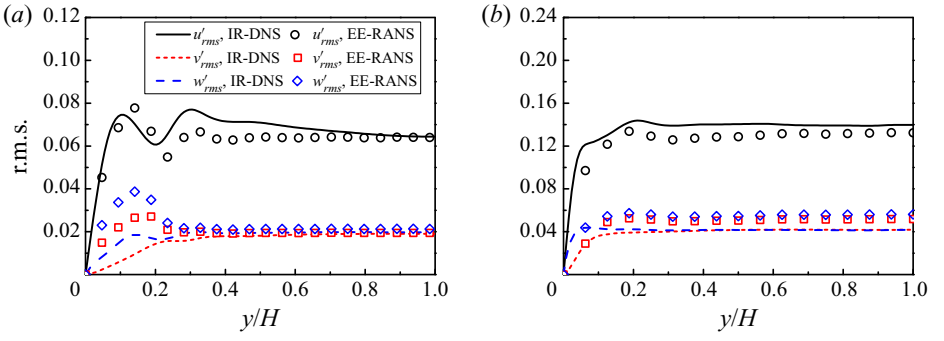


Figure 13. Root-mean-square velocity components from RANS and DNS for (*a*) case 2 ($Re_p = 49.6$) and (*b*) case 3 ($Re_p = 113.5$).

discrepancy in the channel bulk region is higher for Re_p=113.5 than that for Re_p=49.6 in figure 13. We note that there is also a more pronounced discrepancy in the Reynolds shear stress for Re_p=113.5 (figure 16). We leave the improvement of the model in the presence of shear turbulence effects for the near-wall region and the r.m.s.velocities in the bulk region to a future study.

From figures 15 and 16, the fluid mean velocities and Reynolds shear stress from the RANS model also agree well with the DNS results. As Re_p increases from 9.5 to 49.6, the mean velocity profile becomes flatter and the Reynolds shear stress becomes much smaller, which are well captured by the RANS simulations.

https://doi.org/10.1017/jfm.2022.927 Published online by Cambridge University Press

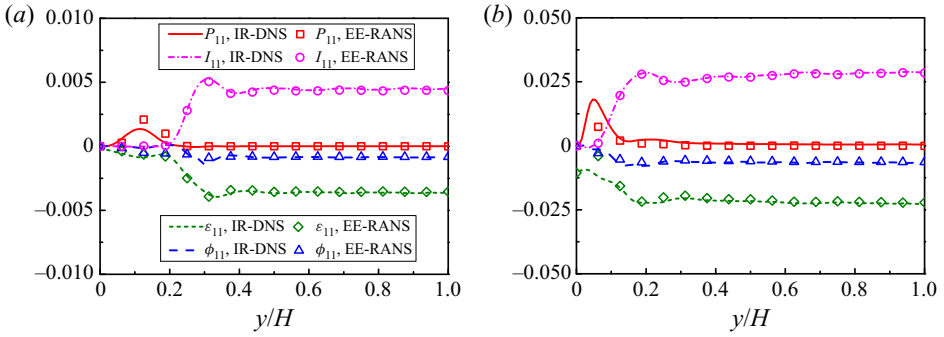


Figure 14. Comparison between RANS and DNS on the selected terms in the equation of $< u_1' u_1' >$ for (*a*) Case 2 ($Re_p = 49.6$), and (*b*) Case 3 ($Re_p = 113.5$). All terms are normalized with $\rho_f u_b^3/H$.

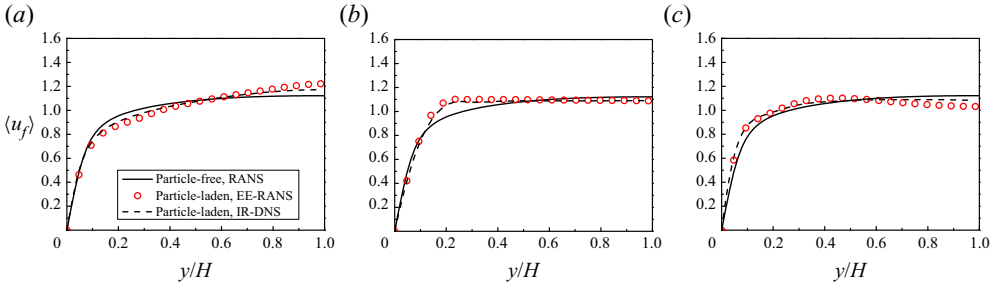


Figure 15. Mean fluid velocity profiles of turbulent channel flows for (*a*) case 1 (upflow, $Re_p = 9.5$), (*b*) case 2 (upflow, $Re_p = 49.6$) and (*c*) case 3 (upflow, $Re_p = 113.5$).

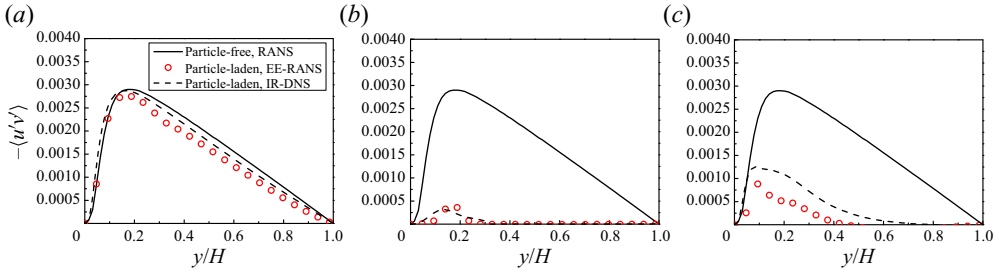


Figure 16. Reynolds shear stress $-\langle u'v' \rangle$ profiles for (*a*) case 1 (upflow, $Re_p = 9.5$), (*b*) case 2 (upflow, $Re_p = 49.6$) and (*c*) case 3 (upflow, $Re_p = 113.5$).

The profiles of TKE for cases 4–6 in table 5 are shown in figure 17. The results show that the RSM also works well for the situations of higher flow Reynolds number, downward flow and high density ratio. Particularly, figures 12(*b*) and 17(*b*) indicate that the effects of flow direction on TKE can be captured by the RANS model: from figure 12(*b*), for upflow at $Re_p = 49.6$ (case 2), the turbulence is significantly suppressed by particles, whereas from figure 17(*b*), for downflow at $Re_p = 38.3$ (case 5), the turbulence is roughly not attenuated by particles, particularly if compared with the DNS result of the single-phase flow (Xia *et al.* 2021). Xia *et al.* (2021) attributed the reason for the difference to the observations that, for case 2, the particles migrate towards the channel centre, and the shear-induced large-scale vortices are significantly suppressed, whereas, for case 5, the

https://doi.org/10.1017/jfm.2022.927 Published online by Cambridge University Press

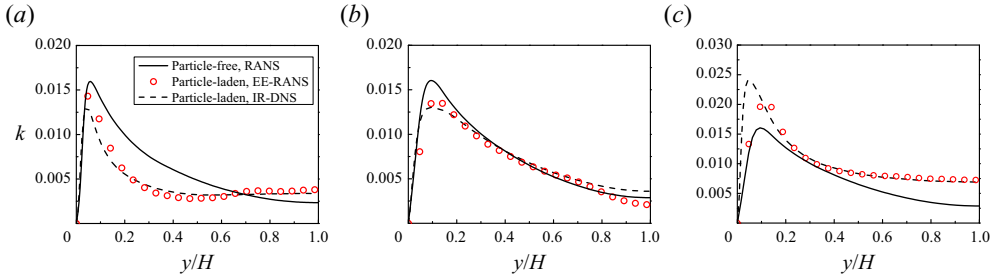


Figure 17. Comparison of the TKE profile predicted by RANS and DNS for (*a*) case 4 (upflow, Re_p=102.1, $Re_b = 12000$), (*b*) case 5 (downflow, Re_p=38.3) and (*c*) case 6 (downflow, $\rho_r = 100$, Re_p=90.6).

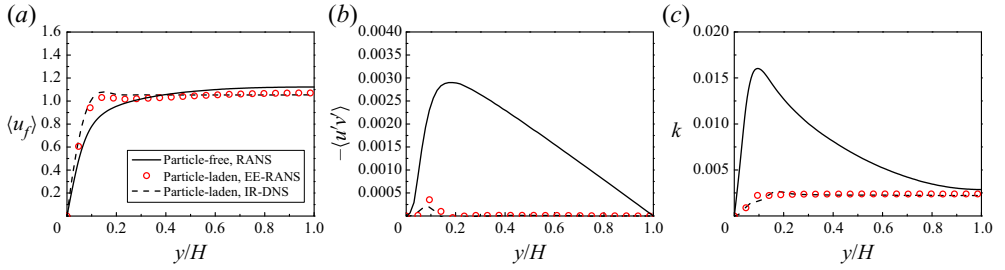


Figure 18. (*a*) Mean fluid velocity, (*b*) Reynolds shear stress $-\langle u'v'\rangle$ and (*c*) TKE profiles predicted for case 9 ($\phi_0 = 14.2\,\%$, $Re_p = 22.9$).

particles migrate towards the channel wall, and the flow is still dominated by large-scale vortices. It is interesting that the RANS simulation does not resolve the vortices, but is able to predict the turbulence attenuation or enhancement quantitatively.

The profiles of mean fluid velocity, Reynolds shear stress $-\langle u'v'\rangle$, as well as TKE for case 9 ($\phi_0 = 14.2\,\%$, Re_p=22.9) in table 5 are shown in figure 18. The results show that our model prediction is still good for larger volume fractions. We note that in the bulk region the shear turbulence is almost completely suppressed by the particles in this case ($\phi_0 = 14.2\,\%$, $Re_p = 22.9$), evidenced by vanishingly small Reynolds shear stress.

In the following we attempt to identify the main reason why the appreciable turbulence attenuation occurs in the RANS simulations for case 2, but not for case 5. Vreman (2015) demonstrated that the non-uniform part of the drag force contributed significantly to the particle-induced turbulence attenuation in point-particle simulations. The same analysis method is used here, with a minor difference that the effect of the particle volume fraction is taken into account, which was not considered by Vreman (2015) for point-particle simulations.

The domain-averaged mean momentum equation of the fluid phase can be derived from (5.5) as

$$-\frac{\tau_w}{H} + \overline{\phi_f}\left(-\frac{\mathrm{d}p_e}{\mathrm{d}x_1}\right) - \overline{F_D} = 0, \tag{5.6}$$

where $\overline{\phi_f}$ and $\overline{F_D}$ are the domain-averaged fluid volume fraction and drag force. If this equation is subtracted from (5.5), we obtain

$$\frac{\mathrm{d}}{\mathrm{d}x_2}\left(\phi_f \mu \frac{\partial\langle u_1\rangle}{\partial x_2}\right) + \phi_f^{nu}\left(-\frac{\mathrm{d}p_e}{\mathrm{d}x_1}\right) + \frac{\mathrm{d}(\phi_f \rho_f \langle -u_1' u_2'\rangle)}{\mathrm{d}x_2} + \frac{\tau_w}{H} - F_D^{nu} = 0, \tag{5.7}$$

https://doi.org/10.1017/jfm.2022.927 Published online by Cambridge University Press

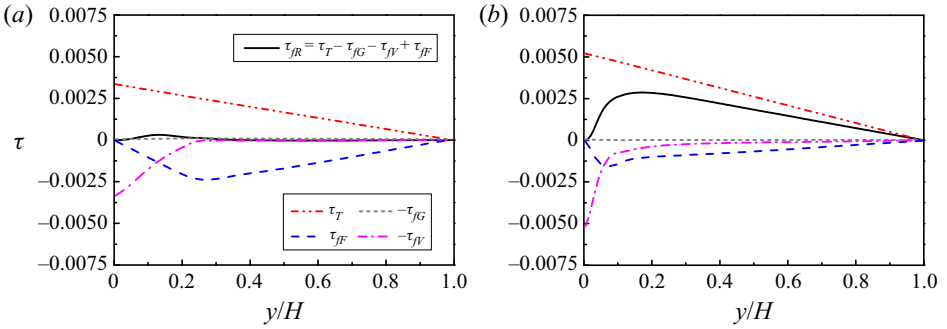


Figure 19. Profiles of the terms defined in (5.8) for (*a*) case 2 (upflow, $Re_p = 49.6$) and (*b*) case 5 (downflow, $Re_p = 38.3$). All terms are normalized by $\rho_f u_b^2$.

where F_D^{nu} and ϕ_f^{nu} are the non-uniform part of the drag and the fluid volume fraction, respectively, i.e. $F_D^{nu} = F_D - \overline{F_D}$ and $\phi_f^{nu} = \phi_f - \overline{\phi_f}$. Integrating (5.7) from the wall ($x_2 = 0$) to $x_2 = y$, we obtain

$$\underbrace{(\phi_f \rho_f \langle -u_1' u_2' \rangle)}_{\tau_{fR}} = \underbrace{\tau_w \left(1 - \frac{y}{H} - \frac{\int_0^y \phi_f^{nu} \,\mathrm{d}x_2}{H} \right)}_{\tau_T} \underbrace{\mp \phi_0 (\rho_s - \rho_f) g \int_0^y \phi_f^{nu} \,\mathrm{d}x_2}_{\tau_G} - \underbrace{\left(\phi_f \mu \frac{\partial \langle u_1 \rangle}{\partial x_2} \right)}_{\tau_{fV}} + \underbrace{\int_0^y F_D^{nu} \,\mathrm{d}x_2}_{\tau_F}. \tag{5.8}$$

Figure 19 shows the profiles of the terms in (5.8) for case 2 and case 5 obtained from the DNS data of Yu *et al.* (2021) and Xia *et al.* (2021). Since the particle volume fraction is low, the term τ_G is negligibly small. The drag force term τ_F is negative for both cases 2 and 5, which means that the drag tends to attenuate the fluid Reynolds stress, from (5.8). For case 2, the interphase drag is larger in the channel centre region due to particle migration towards the channel centre and thereby a higher particle volume fraction there (Yu *et al.* 2021), which leads to the integration term of the non-uniform force τ_F having a larger negative value in the bulk region, compared with case 5. Therefore, the non-uniform drag distribution is responsible for the turbulence attenuation, as pointed out by Vreman (2015). The turbulence enhancement at relatively high particle Reynolds numbers is clearly caused by the TKE interfacial term I_k. The accuracy of the interfacial term models is important to the quantitative prediction of the turbulence attenuation and enhancement. One advantage of the RSM over the eddy viscosity model for the multiphase flow is that the effect of the interphase drag on the Reynolds shear stress can be adequately accounted for by the former.

We also compare our RANS results on TKE and the r.m.s.velocities to the DNS results of Uhlmann (2008) and Santarelli *et al.* (2016) in figure 20, and good agreement can be seen.

https://doi.org/10.1017/jfm.2022.927 Published online by Cambridge University Press

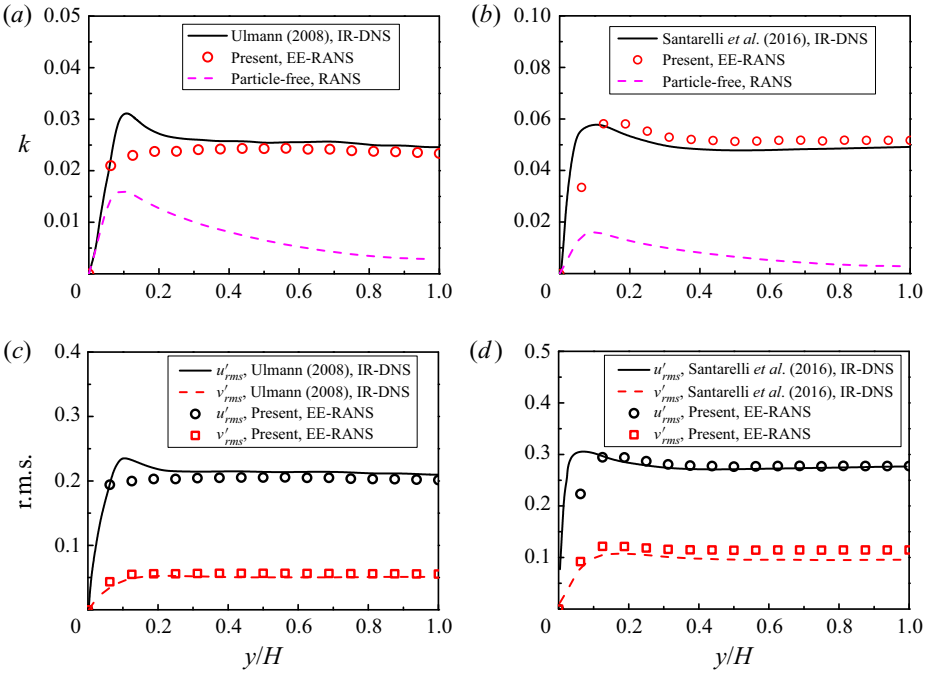


Figure 20. Comparison between the present RANS results, TKE and the r.m.s. velocities and the IR-DNS results of (*a*,*c*) Uhlmann (2008), case 7, and (*b*,*d*) Santarelli *et al.* (2016), case 8.

6. Conclusions

Based on data from the IR-DNS of particle sedimentation in a periodic domain at a density ratio ranging from 0.01 to 1000, a particle concentration ranging from 2.3 % to 30.2 % and a particle Reynolds number below 250, the novel models for the particle-induced interfacial terms for the second-moment closure have been developed. The main conclusions are drawn as follows.

(i) The interfacial term in the dissipation rate equation is modelled as

$$I_\varepsilon = C_{\varepsilon 3}\frac{\nu}{d_p^2}I_k, \tag{6.1}$$

where I_k is the interfacial term in the TKE equation modelled as $I_k = F_D u_r$, and the coefficient $C_{\varepsilon 3}$ is modelled as

$$\frac{C_{\varepsilon 3}}{C_{\varepsilon 2}} = Re_p\frac{d_p F_D}{(1-\phi)\rho_f(k/u_r^2)u_r^2}. \tag{6.2}$$

In (6.2) the relative TKE k/u_r^2 is modelled as

$$\frac{k}{u_r^2} = 0.92\rho_r^{-0.02}\phi^{0.78} + 0.05\phi^{0.3}(1-\phi)(Re_p/200)^{1.1} + 25\phi^2(\rho_r+0.5)^{-0.15}(1-\phi)^3\exp(-\phi^{1/2}(1-\phi)^{1/2}Re_p{}^{1/2}). \tag{6.3}$$

The correlation for the mean drag coefficient ($F_D = \beta u_r$) is as follows.

https://doi.org/10.1017/jfm.2022.927 Published online by Cambridge University Press

For $\phi \leq 0.1$,

$$\beta_1 = \frac{3}{4} C_d \frac{\rho_f \phi (1-\phi) u_r}{d_p} (1-\phi)^{-n}, \tag{6.4}$$

where C_d is the modified drag coefficient

$$C_d = \frac{24}{(1-\phi)Re_p} (1 + 0.15((1-\phi)Re_p)^{0.687}), \tag{6.5}$$

and n is the exponent of the correction function in the form

$$n = (3.88 - 0.38 \ln(Re_p)) \ln(\phi^{-1}) \rho_r^{-0.038}. \tag{6.6}$$

For $\phi > 0.1$,

$$\begin{aligned} \beta_2 = {} & 180 \frac{\mu \phi^2}{d_p^2 (1-\phi)} + 18 \frac{\mu (1-\phi)^3 \phi (1 + 1.5\sqrt{\phi})}{d_p^2} \\ & + \frac{18 \mu \phi (1-\phi) Re_m}{d_p^2} \left[0.11\phi(1+\phi) - \frac{0.00456}{(1-\phi)^4} + \left(0.169(1-\phi) \right.\right. \\ & \left.\left. + \frac{0.0644}{(1-\phi)^4} \right) Re_m^{-0.343} \right] + 2.76 Re_m^{0.8} \rho_r^{-0.05} \frac{\mu \phi^2}{d_p^2 (1-\phi)}. \end{aligned} \tag{6.7}$$

(ii) The particle-induced force term in the pressure–strain terms is modelled as $\Phi_{ij,3} = -C_3(I_{ij} - \frac{2}{3} I_k \delta_{ij})$, with the coefficient C_3 correlated with

$$C_3(\phi, Re_p) = \phi + aRe_p + bRe_p^2 + c, \tag{6.8}$$

in which $a = 3.723 \times 10^{-4}$, $b = 2.819 \times 10^{-6}$ and $c = -0.010$. The interfacial term in the Reynolds stress equation is modelled as $I_{ij} = F_{Di} u_{rj} + F_{Dj} u_{ri}$, and for the sedimentation system, an only non-zero component is $I_{11} = 2I_k$.

(iii) The anisotropic model for the dissipation rate tensor

$$\varepsilon_{ij} = \phi_f \rho_f \left(f_s \frac{\langle u_i' u_j' \rangle}{k} + \frac{2}{3} (1 - f_s) \delta_{ij} \right) \varepsilon, \tag{6.9}$$

with $f_s = 0.9$, is in excellent agreement with our DNS data on the particle-laden turbulent channel flows.

(iv) The fluid-phase RSM for the particle-laden flows is established with the original RSM for the single-phase flow and the above models for the particle-induced source terms, and is found to be able to quantitatively predict the turbulence enhancement or suppression by particles in vertical channel flows, through the comparison between the RSM-based RANS simulations and the IR-DNS data in the literature. It is shown that the non-uniform drag distribution is responsible for the turbulence attenuation in the upward channel flow. We think that the capability to account for the effect of the drag on the Reynolds stress is the advantage of the RSM over the eddy viscosity model for the particle-laden flows.

Since our correlations are obtained from the sedimentation system, they are suited to the case where the particle sedimentation effect (or the interphase mean slip velocity) exist. For convenience, we assume that the coefficients in the single-phase

https://doi.org/10.1017/jfm.2022.927 Published online by Cambridge University Press

		$d_p/\Delta x = 12.8$	$d_p/\Delta x = 25.6$	$d_p/\Delta x = 51.2$
$\phi = 2.36\,\%$	u_r/u_c	1.036	1.084	1.094
	k/u_r^2	0.059	0.062	0.063
$\phi = 14.2\,\%$	u_r/u_c	0.627	0.661	0.670
	k/u_r^2	0.225	0.219	0.223

Table 7. Effects of grid resolution on the mean relative velocity and TKE normalized with u_c at $Ga = 170$, $L/d_p = 5$ and $\rho_r = 2$. $u_c = \sqrt{4d_p(\rho_r - 1)g/3}$.

		$L/d_p = 5$	$L/d_p = 10$	$L/d_p = 20$
$Ga = 73$	u_r/u_c	0.518	0.529	0.533
	k/u_r^2	0.215	0.231	0.233
$Ga = 170$	u_r/u_c	0.661	0.697	0.714
	k/u_r^2	0.207	0.207	0.208

Table 8. Effects of the domain size on the mean relative velocity and TKE normalized with u_c at $\phi = 14.2\,\%$, $d_p/\Delta x = 25.6$ and $\rho_r = 2$.

RSM are not modified by the particles. Based on DNS data, extensive studies on the full two-fluid RSM can be conducted in the future, such as the lift force model, the solid-phase stress model and how the coefficients in the single-phase RSM are modified by the particles.

Funding. The work was supported by the National Natural Science Foundation of China (grant nos 12072319, 91752117 and 91852205).

Declaration of interests. The authors report no conflict of interest.

Author ORCIDs.
Zhaosheng Yu https://orcid.org/0000-0001-8999-407X;
Yu Guo https://orcid.org/0000-0002-0012-4498.

Appendix A. Box size and mesh resolution validations

The DF/FD solver has been extensively validated in our previous studies for the turbulent channel flows (Wang *et al.* 2016; Yu *et al.* 2016, 2019, 2021) and particle sedimentation (Yu & Shao 2007; Shao, Wu & Yu 2012; Xia *et al.* 2022*b*). It was shown that the mesh resolution of $d_p/\Delta x = 12.8$ is able to predict with reasonable accuracy the settling velocity of a single particle at relatively low particle Reynolds numbers (e.g. $Re_p < 100$) (Shao *et al.* 2012; Xia *et al.* 2022*b*). Here we perform a mesh convergence test for the sedimentation of many particles at relatively high particle Reynolds numbers. The time step is determined from a fixed Courant–Friedrichs–Lewy (CFL) number CFL ≈ 0.15, where the CFLnumber is defined as CFL $= u_c \Delta t/\Delta x$. The results of the mesh convergence test on the mean relative slip u_r/u_c and the relative TKE k/u_r^2 at $Ga = 170$ ($Re_p \approx 210$ for $\phi = 2.3\,\%$) are presented in table 7, which shows that the relative differences in both mean velocity and TKE obtained with $d_p/\Delta x = 25.6$ and 51.2 are below 1.5 %. Limited by our computational resource, the mesh resolution of $d_p/\Delta x = 25.6$ is chosen for our simulations.

https://doi.org/10.1017/jfm.2022.927 Published online by Cambridge University Press

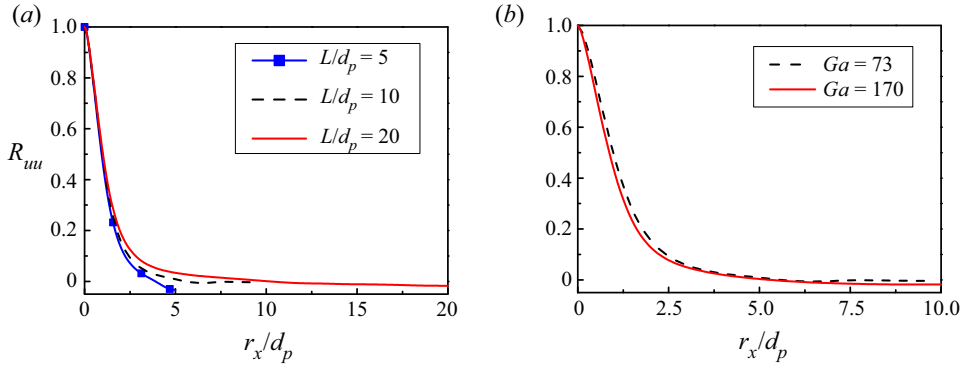


Figure 21. (*a*) Two-point correlation function of vertical fluid velocity as a function of vertical separation distance for different domain sizes at $\phi = 14.2\,\%$ and $Ga = 73$, (*b*) fluid velocity correlation functions for $Ga = 73$ and 170 at $\phi = 14.2\,\%$, $L/d_p = 10$ and $\rho_r = 2$.

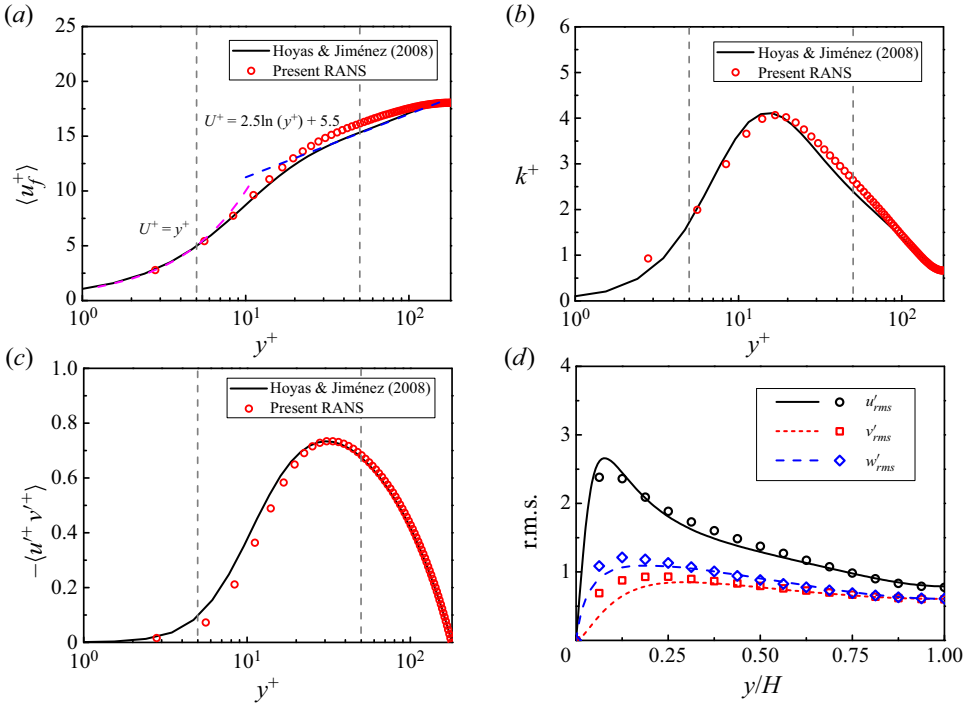


Figure 22. Comparison between the near-wall RSM-based RANS simulations and the DNS results of Hoyas & Jiménez (2008) for the particle-free turbulent channel flow at $Re_\tau = 180$. (*a*) Mean velocity, (*b*) TKE, (*c*) Reynolds shear stress and (*d*) r.m.s. velocities. The lines and the symbols represent the DNS results of Hoyas & Jiménez (2008) and the present RANS results, respectively.

In addition, we examine the dependence of the results on the domain size. The results on the effects of the domain size on the mean relative velocity and TKE normalized with u_c at $\phi = 14.2\,\%$, $d_p/\Delta x = 25.6$ and $\rho_r = 2$ are presented in table 8, which indicates that both mean relative velocity and TKE increase slightly with increasing domain size, and they change little as the domain size is increased beyond $L/d_p = 10$.

https://doi.org/10.1017/jfm.2022.927 Published online by Cambridge University Press

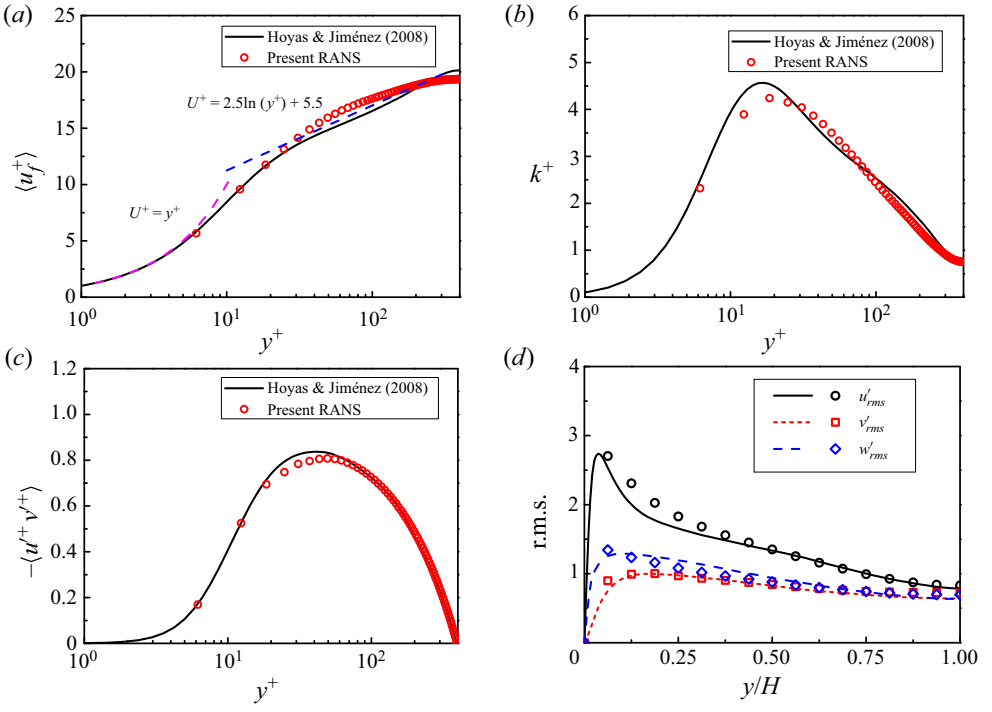


Figure 23. Comparison between the near-wall RSM-based RANS simulations and the DNS results of Hoyas & Jiménez (2008) for the particle-free turbulent channel flow at $Re_\tau = 395$. (*a*) Mean velocity, (*b*) TKE, (*c*) Reynolds shear stress and (*d*) r.m.s. velocities. The lines and the symbols represent the DNS results of Hoyas & Jiménez (2008) and the present RANS results, respectively.

The two-point autocorrelation function for the vertical component of the fluid fluctuating velocity as a function of vertical separation distance can be computed from

$$R_{uu}(r_x) = \frac{\langle \overline{u'(x, y, z, t)u'(x + r_x, y, z, t)} \rangle}{\langle \overline{u'(x, y, z, t)^2} \rangle}. \tag{A1}$$

Figure 21(*a*) shows the velocity correlation functions for different domain sizes at $Ga = 73$ ($Re_p \approx 44$) and $\phi = 14.2\,\%$. The results show that the two-point correlations vanish at the separation of half-domain height for $L/d_p = 10$ and 20. The velocity correlation function for $Ga = 170$ ($Re_p \approx 137$) and $\phi = 14.2\,\%$ at $L/d_p = 10$ is shown in figure 21(*b*), and no correlation is observed at the separation of half-domain height, unlike the dilute case where strong clustering of particles in the form of vertically elongated columnar regions were observed by Uhlmann & Doychev (2014) at $Ga = 178$. The results on the two-point autocorrelation function and the settling velocity above indicate that a domain size of $L/d_p = 10$ is sufficiently large to ensure a rough independence of the results on the domain size. Nevertheless, some results for $L/d_p = 5$ (denoted as the 'small' case) are also reported, as compared with those for $L/d_p = 10$ (denoted as the 'large' case), since the small size of the computational cell may also be used for two-fluid RANS simulations. Unless otherwise specified, the results reported are obtained with $L/d_p = 10$.

https://doi.org/10.1017/jfm.2022.927 Published online by Cambridge University Press

Appendix B. RANS simulations of fully developed particle-free turbulent channel flows

The test cases are the particle-free turbulent channel flows at $Re_\tau = 180$ and 395. Here Re_τ is the friction Reynolds number defined by $Re_\tau = u_\tau H/\nu$ ($u_\tau = \tau_w/\rho_f$ being the wall friction velocity and τ_w being the mean shear stress on the walls).

Profiles of the fluid mean velocity, TKE, Reynolds shear stress and r.m.s. velocities are compared with the benchmark DNS data of Hoyas & Jiménez (2008) in figures 22 and 23. From these figures, our results obtained from the near-wall RSM are in good agreement with those of Hoyas & Jiménez (2008).

References

Anderson, T.B. & Jackson, R. 1967 Fluid mechanical description of fluidized beds. Equations of motion. *Ind. Engng Chem. Fundam.* **6** (4), 527–539.

Ansys, Inc. 2013 *ANSYS FLUENT theory guide. Release 15.0*. Canonsburg.

Antal, S.P., Lahey Jr, R.T. & Flaherty, J.E. 1991 Analysis of phase distribution in fully developed laminar bubbly two-phase flow. *Intl J. Multiphase Flow* **17** (5), 635–652.

Baker, M.C., Fox, R.O., Kong, B., Capecelatro, J. & Desjardins, O. 2020 Reynolds-stress modeling of cluster-induced turbulence in particle-laden vertical channel flow. *Phys. Rev. Fluids* **5** (7), 074304.

Balachandar, S. & Eaton, J.K. 2010 Turbulent dispersed multiphase flow. *Annu. Rev. Fluid Mech.* **42**, 111–133.

Barnocky, G. & Davis, R.H. 1988 Elastohydrodynamic collision and rebound of spheres: experimental verification. *Phys. Fluids* **31** (6), 1324–1329.

Burns, A.D., Frank, T., Hamill, I. & Shi, J.M. 2004 The favre averaged drag model for turbulent dispersion in Eulerian multi-phase flows. In *5th International Conference on Multiphase Flow, ICMF*, vol. 4, pp. 1–17. ICMF.

Capecelatro, J., Desjardins, O. & Fox, R.O. 2016*a* Strongly coupled fluid-particle flows in vertical channels. I. Reynolds-averaged two-phase turbulence statistics. *Phys. Fluids* **28** (3), 033306.

Capecelatro, J., Desjardins, O. & Fox, R.O. 2016*b* Strongly coupled fluid-particle flows in vertical channels. II. Turbulence modeling. *Phys. Fluids* **28** (3), 033307.

Cokljat, D., Slack, M., Vasquez, S.A., Bakker, A. & Montante, G. 2006 Reynolds-stress model for Eulerian multiphase. *Prog. Comput. Fluid Dyn. Intl J.* **6** (1–3), 168–178.

Colombo, M. & Fairweather, M. 2015 Multiphase turbulence in bubbly flows: RANS simulations. *Intl J. Multiphase Flow* **77**, 222–243.

Crowe, C.T., Schwarzkopf, J.D., Sommerfeld, M. & Tsuji, Y. 2011 *Multiphase Flows with Droplets and Particles*. CRC Press.

Crowe, C.T., Troutt, T.R. & Chung, J.N. 1996 Numerical models for two-phase turbulent flows. *Annu. Rev. Fluid Mech.* **28** (1), 11–43.

Deen, N.G., Van Sint Annaland, M., Van der Hoef, M.A. & Kuipers, J.A.M. 2007 Review of discrete particle modeling of fluidized beds. *Chem. Engng Sci.* **62** (1–2), 28–44.

Ding, J. & Gidaspow, D. 1990 A bubbling fluidization model using kinetic theory of granular flow. *AIChE J.* **36** (4), 523–538.

Du Cluzeau, A., Bois, G. & Toutant, A. 2019 Analysis and modelling of Reynolds stresses in turbulent bubbly up-flows from direct numerical simulations. *J. Fluid Mech.* **866**, 132–168.

Fox, R.O. 2014 On multiphase turbulence models for collisional fluid–particle flows. *J. Fluid Mech.* **742**, 368–424.

Gidaspow, D. 1994 *Multiphase Flow and Fluidization: Continuum and Kinetic Theory Descriptions*. Academic Press.

Glowinski, R., Pan, T.-W., Hesla, T.I. & Joseph, D.D. 1999 A distributed lagrange multiplier/fictitious domain method for particulate flows. *Intl J. Multiphase Flow* **25** (5), 755–794.

Hanjalić, K. & Launder, B.E. 1976 Contribution towards a Reynolds-stress closure for low-Reynolds-number turbulence. *J. Fluid Mech.* **74** (4), 593–610.

Hanjalić, K. & Launder, B. 2011 *Modelling Turbulence in Engineering and the Environment: Second-Moment Routes to Closure*. Cambridge University Press.

Hoyas, S. & Jiménez, J. 2008 Reynolds number effects on the Reynolds-stress budgets in turbulent channels. *Phys. Fluids* **20** (10), 101511.

https://doi.org/10.1017/jfm.2022.927 Published online by Cambridge University Press

ISHII, M. & HIBIKI, T. 2010 *Thermo-Fluid Dynamics of Two-Phase Flow*. Springer Science & Business Media.

JEFFREY, D.J. 1982 Low-Reynolds-number flow between converging spheres. *Mathematika* **29** (1), 58–66.

JOSHI, J.B. & NANDAKUMAR, K. 2015 Computational modeling of multiphase reactors. *Annu. Rev. Chem. Biomol. Engng* **6**, 347–378.

KATAOKA, I., BESNARD, D.C. & SERIZAWA, A. 1992 Basic equation of turbulence and modeling of interfacial transfer terms in gas-liquid two-phase flow. *Chem. Engng Commun.* **118** (1), 221–236.

KIM, J., MOIN, P. & MOSER, R. 1987 Turbulence statistics in fully developed channel flow at low Reynolds number. *J. Fluid Mech.* **177**, 133–166.

LU, H., GIDASPOW, D., BOUILLARD, J. & LIU, W. 2003 Hydrodynamic simulation of gas–solid flow in a riser using kinetic theory of granular flow. *Chem. Engng J.* **95** (1–3), 1–13.

LUMLEY, J.L. 1979 Computational modeling of turbulent flows. *Adv. Appl. Mech.* **18**, 123–176.

MA, T., LUCAS, D. & BRAGG, A.D. 2020*a* Explicit algebraic relation for calculating Reynolds normal stresses in flows dominated by bubble-induced turbulence. *Phys. Rev. Fluids* **5** (8), 084305.

MA, T., LUCAS, D., JAKIRLIĆ, S. & FRÖHLICH, J. 2020*b* Progress in the second-moment closure for bubbly flow based on direct numerical simulation data. *J. Fluid Mech.* **883**, A9.

MA, T., SANTARELLI, C., ZIEGENHEIN, T., LUCAS, D. & FRÖHLICH, J. 2017 Direct numerical simulation–based Reynolds-averaged closure for bubble-induced turbulence. *Phys. Rev. Fluids* **2** (3), 034301.

MANSOUR, N.N., KIM, J. & MOIN, P. 1988 Reynolds-stress and dissipation-rate budgets in a turbulent channel flow. *J. Fluid Mech.* **194**, 15–44.

MASOOD, R.M.A., RAUH, C. & DELGADO, A. 2014 CFD simulation of bubble column flows: an explicit algebraic Reynolds stress model approach. *Intl J. Multiphase Flow* **66**, 11–25.

MAXEY, M. 2017 Simulation methods for particulate flows and concentrated suspensions. *Annu. Rev. Fluid Mech.* **49**, 171–193.

MEHRABADI, M., TENNETI, S., GARG, R. & SUBRAMANIAM, S. 2015 Pseudo-turbulent gas-phase velocity fluctuations in homogeneous gas-solid flow: fixed particle assemblies and freely evolving suspensions. *J. Fluid Mech.* **770**, 210–246.

NAOT, D. 1970 Interactions between components of the turbulent velocity correlation tensor. *Isr. J. Technol.* **8**, 259–269.

PENG, C., AYALA, O.M. & WANG, L.P. 2019 A direct numerical investigation of two-way interactions in a particle-laden turbulent channel flow. *J. Fluid Mech.* **875**, 1096–1144.

POELMA, C., WESTERWEEL, J. & OOMS, G. 2007 Particle–fluid interactions in grid-generated turbulence. *J. Fluid Mech.* **589**, 315–351.

POLITANO, M.S., CARRICA, P.M. & CONVERTI, J. 2003 A model for turbulent polydisperse two-phase flow in vertical channels. *Intl J. Multiphase Flow* **29** (7), 1153–1182.

RIELLA, M., KAHRAMAN, R. & TABOR, G.R. 2019 Inhomogeneity and anisotropy in Eulerian–Eulerian near-wall modelling. *Intl J. Multiphase Flow* **114**, 9–18.

RISSO, F., ROIG, V., AMOURA, Z., RIBOUX, G. & BILLET, A.M. 2008 Wake attenuation in large Reynolds number dispersed two-phase flows. *Phil. Trans. R. Soc.* A*: Math. Phys. Engng Sci.* **366** (1873), 2177–2190.

ROTTA, J.C. 1951 Statistische theorie nichthomogener turbulenz. *Z. Phys.* **129** (6), 547–572.

RZEHAK, R. & KREPPER, E. 2013 CFD modeling of bubble-induced turbulence. *Intl J. Multiphase Flow* **55**, 138–155.

SAFFMAN, P.G. 1956 On the motion of small spheroidal particles in a viscous liquid. *J. Fluid Mech.* **1** (5), 540–553.

SANTARELLI, C. & FRÖHLICH, J. 2015 Direct numerical simulations of spherical bubbles in vertical turbulent channel flow. *Intl J. Multiphase Flow* **75**, 174–193.

SANTARELLI, C., ROUSSEL, J. & FRÖHLICH, J. 2016 Budget analysis of the turbulent kinetic energy for bubbly flow in a vertical channel. *Chem. Engng Sci.* **141**, 46–62.

SATO, Y. & HISHIDA, K. 1996 Transport process of turbulence energy in particle-laden turbulent flow. *Intl J. Heat Fluid Flow* **17** (3), 202–210.

SATO, Y., SADATOMI, M. & SEKOGUCHI, K. 1981 Momentum and heat transfer in two-phase bubble flow–I. Theory. *Intl J. Multiphase Flow* **7** (2), 167–177.

SCHWARZKOPF, J.D., CROWE, C.T. & DUTTA, P. 2009 A turbulence dissipation model for particle laden flow. *AIChE J.* **55** (6), 1416–1425.

SHAO, X., WU, T. & YU, Z. 2012 Fully resolved numerical simulation of particle-laden turbulent flow in a horizontal channel at a low Reynolds number. *J. Fluid Mech.* **693**, 319–344.

SHI, P. & RZEHAK, R. 2020 Solid-liquid flow in stirred tanks: Euler-Euler/RANS modeling. *Chem. Engng Sci.* **227**, 115875.

https://doi.org/10.1017/jfm.2022.927 Published online by Cambridge University Press

SHIR, C.C. 1973 A preliminary numerical study of atmospheric turbulent flows in the idealized planetary boundary layer. *J. Atmos. Sci.* **30** (7), 1327–1339.

SO, R.M.C., AKSOY, H., YUAN, S.P. & SOMMER, T.P. 1996 Modeling Reynolds-number effects in wall-bounded turbulent flows. *Trans. ASME J. Fluids Engng* **118** (2), 260–267.

SPEZIALE, C.G., SARKAR, S. & GATSKI, T.B. 1991 Modelling the pressure–strain correlation of turbulence: an invariant dynamical systems approach. *J. Fluid Mech.* **227**, 245–272.

TANG, Y., PETERS, E.A.J.F., KUIPERS, J.A.M., KRIEBITZSCH, S.H.L. & VAN DER HOEF, M.A. 2015 A new drag correlation from fully resolved simulations of flow past monodisperse static arrays of spheres. *AIChE J.* **61** (2), 688–698.

TENNETI, S. & SUBRAMANIAM, S. 2014 Particle-resolved direct numerical simulation for gas-solid flow model development. *Annu. Rev. Fluid Mech.* **46**, 199–230.

TROSHKO, A.A. & HASSAN, Y.A. 2001 A two-equation turbulence model of turbulent bubbly flows. *Intl J. Multiphase Flow* **27** (11), 1965–2000.

TSUJI, Y., KAWAGUCHI, T. & TANAKA, T. 1993 Discrete particle simulation of two-dimensional fluidized bed. *Powder Technol.* **77** (1), 79–87.

TSUJI, Y., TANAKA, T. & ISHIDA, T. 1992 Lagrangian numerical simulation of plug flow of cohesionless particles in a horizontal pipe. *Powder Technol.* **71** (3), 239–250.

UHLMANN, M. 2008 Interface-resolved direct numerical simulation of vertical particulate channel flow in the turbulent regime. *Phys. Fluids* **20** (5), 053305.

UHLMANN, M. & DOYCHEV, T. 2014 Sedimentation of a dilute suspension of rigid spheres at intermediate Galileo numbers: the effect of clustering upon the particle motion. *J. Fluid Mech.* **752**, 310–348.

VREMAN, A.W. 2015 Turbulence attenuation in particle-laden flow in smooth and rough channels. *J. Fluid Mech.* **773**, 103–136.

WANG, L.P., PENG, C., GUO, Z. & YU, Z. 2016 Flow modulation by finite-size neutrally buoyant particles in a turbulent channel flow. *J. Fluids Engng* **138** (4), 041306.

WEN, C.Y. & YU, Y.H. 1966 Mechanics of fluidization. In *Chemical Engineering Progress Symposium Series*, vol. 62, pp. 100–111.

XIA, Y., LIN, Z., PAN, D. & YU, Z. 2021 Turbulence modulation by finite-size heavy particles in a downward turbulent channel flow. *Phys. Fluids* **33** (6), 063321.

XIA, Y., YU, Z., LIN, Z. & GUO, Y. 2022*a* Model of interfacial term in turbulent kinetic energy equation and computation of dissipation rate for particle-laden flows. *Phys. Fluids* **34** (8), 083311.

XIA, Y., YU, Z., PAN, D., LIN, Z. & GUO, Y. 2022*b* Drag model from interface-resolved simulations of particle sedimentation in a periodic domain and vertical turbulent channel flows. *J. Fluid Mech.* **944**, A25.

YAO, W. & MOREL, C. 2004 Volumetric interfacial area prediction in upward bubbly two-phase flow. *Intl J. Heat Mass Transfer* **47** (2), 307–328.

YU, Z., LIN, Z., SHAO, X. & WANG, L.P. 2016 A parallel fictitious domain method for the interface-resolved simulation of particle-laden flows and its application to the turbulent channel flow. *Engng Appl. Comput. Fluid Mech.* **10** (1), 160–170.

YU, Z. & SHAO, X. 2007 A direct-forcing fictitious domain method for particulate flows. *J. Comput. Phys.* **227** (1), 292–314.

YU, Z., XIA, Y., GUO, Y. & LIN, J. 2021 Modulation of turbulence intensity by heavy finite-size particles in upward channel flow. *J. Fluid Mech.* **913**, A3.

YU, Z., ZHU, C., WANG, Y. & SHAO, X. 2019 Effects of finite-size neutrally buoyant particles on the turbulent channel flow at a Reynolds number of 395. *Appl. Math. Mech.* **40** (2), 293–304.

ZHU, H.P., ZHOU, Z.Y., YANG, R.Y. & YU, A.B. 2007 Discrete particle simulation of particulate systems: theoretical developments. *Chem. Engng Sci.* **62** (13), 3378–3396.

https://doi.org/10.1017/jfm.2022.927 Published online by Cambridge University Press